Analytical relationships for 2D Re-entrant auxetic metamaterials
An application to 3D printing flexible implants

Hedayati, Reza; Yousefi, Armin; Dezaki, Mohammadreza Lalegani; Bodaghi, Mahdi

DOI
10.1016/j.jmbbm.2023.105938

Publication date
2023

Document Version
Final published version

Published in
Journal of the mechanical behavior of biomedical materials

journal of the mechanical behavior of biomedical materials 143 (2023) 105938

Contents lists available at ScienceDirect

Journal of the Mechanical Behavior of Biomedical Materials

journal homepage: www.elsevier.com/locate/jmbbm

Analytical relationships for 2D Re-entrant auxetic metamaterials: An application to 3D printing flexible implants

Reza Hedayati [a], Armin Yousefi [b], Mohammadreza Lalegani Dezaki [b], Mahdi Bodaghi [b,*]

[a] Department of Aerospace Materials and Structures (ASM), Faculty of Aerospace Engineering, Delft University of Technology (TU Delft), Kluyverweg 1, 2629, HS, Delft, the Netherlands

[b] Department of Engineering, School of Science and Technology, Nottingham Trent University, Nottingham, NG11 8NS, UK

ARTICLE INFO

Keywords:
Negative Poisson's ratio
Analytical solution
Re-entrant
Achilles tendon
3D printing
Metamaterials

ABSTRACT

Both 2D and 3D re-entrant designs are among the well-known prevalent auxetic structures exhibiting negative Poisson's ratio. The present study introduces novel analytical relationships for 2D re-entrant hexagonal honeycombs for both negative and positive ranges of the cell interior angle θ ($\theta < 0$ showing a negative Poisson's ratio). The derived analytical solutions are validated against finite element method (FEM) and experimental results. The results show that, compared to the analytical solutions available in the literature, the analytical relationships presented in this study provide the most accurate results for elastic modulus, Poisson's ratio, and yield stress. The analytical/computational tools are then implemented for designing Kinesio taping (KT) structures applicable to treatment of Achilles tendon injuries. One of the main features of the Achilles tendon is a natural auxetic behavior. Poisson's ratio distribution of an Achilles tendon is obtained using longitudinal and transverse strains and are then used to design and 3D print thermoplastic polyurethane (TPU) KT structures with non-uniform distribution of auxetic unit cells. The presented novel KT shows that it is capable of replicating the deformation and global and local Poisson's ratio distributions, similar to those of the Achilles tendon. Due to the absence of similar formulations and procedures in the literature, the results are expected to be instrumental for designing and 3D printing of flexible implants with unusual auxeticity.

1. Introduction

In recent decades, metamaterials have emerged as novel artificial materials with unique properties rarely found in nature (Hedayati and Lakshmanan, 2020; Nicolaou and Motter, 2012; Yousefi et al., Bodaghi; Hedayati et al., 2021a; Roudbarian et al., 2022). Mechanical metamaterials have exceptional mechanical behavior, such as negative Poisson's ratio (NPR) (Yousefi et al., Bodaghi; Rafsanjani and Pasini, 2016; Ghavidelnia et al., 2021; Cheng et al., 2022; Chen et al., 2020; Warner et al., 2017; Kolken et al., 2020), negative stiffness, and fluid-like behaviour. Unlike natural materials, the materials with negative Poisson's ratio also known as auxetics shrink laterally when subjected to compressive loads. Negative Poisson's ratio metamaterials have many applications in industry such as actuators, clothing, energy absorption, and devices with high indentation resistance (Kolken and Zadpoor, 2017; Ghavidelnia et al., 2020a; Hedayati et al., 2023). Since metamaterials can deform with various mechanisms in transverse direction, they are good potential candidates to be used as building blocks of actuators (Hedayati et al., 2018; Sedal et al., 2018; Pan et al., 2020).

Recently, many different auxetic designs such as re-entrant (Evans and Alderson, 2000; Wang et al., 2019), rotating semi-rigid (Wang and Hu, 2014; Slann et al., 2015), chiral (Alderson et al., 2010; Lorato et al., 2010; Huang et al., 2016), horseshoe-shaped (Serjouei et al., 2022) and origami-based (Lv et al., 2014; Kamrava et al., 2017) auxetics have been developed in response to growing industrial demands. Among the developed auxetic designs, the 2D re-entrant auxetic design (Fig. 1c), is the most common auxetic structure. Several studies have investigated the stiffness (Whitty et al., 2002), large deformation behavior (Wan et al., 2004), and shear properties (Fu et al., 2016) of 2D re-entrant structures experimentally, numerically, and analytically. It is well known that analytical solutions provide reliable and inexpensive tools to investigate different properties of auxetic re-entrant structures (Ghavidelnia et al., 2020b).

One of the main applications of 2D re-entrant unit cells is manufacturing hard (Kolken et al., 2018, 2021) and soft (Gupta et al., 2022; Meeusen et al., 2022a) biomedical implants and endovascular

* Corresponding author.
E-mail address: mahdi.bodaghi@ntu.ac.uk (M. Bodaghi).

https://doi.org/10.1016/j.jmbbm.2023.105938
Received 26 March 2023; Received in revised form 12 May 2023; Accepted 24 May 2023
Available online 25 May 2023

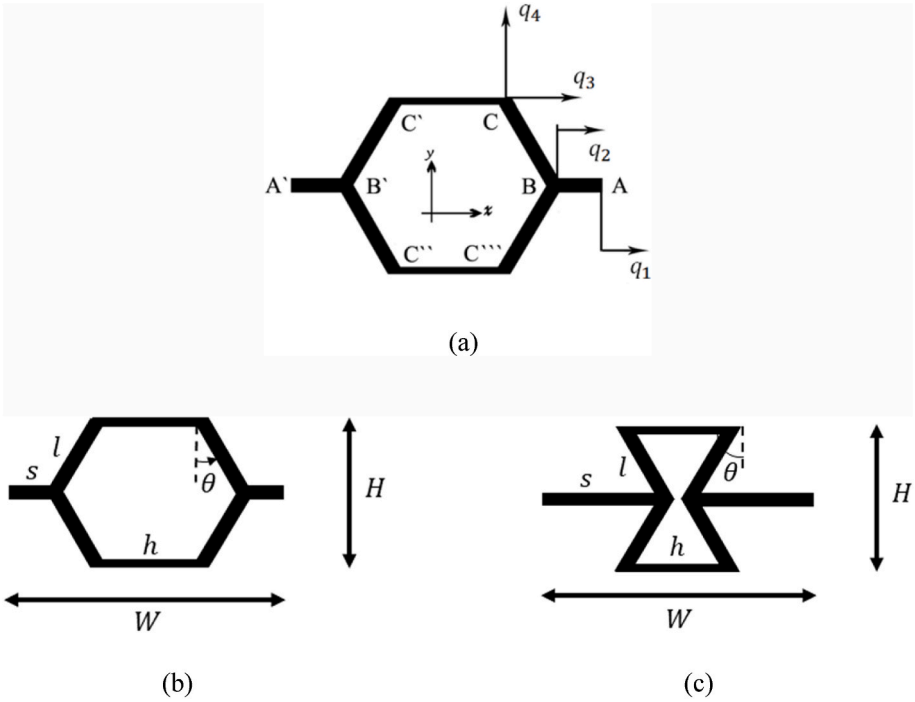

Fig. 1. (a) DOFs of a unit cell, (b) hexagonal unit cells configuration, (c) re-entrant unit cells configuration.

stents (Vellaparambil et al., 2023), (Wanniarachchi et al., 2022). The Achilles tendon is a collagenous connective tissue that connects the gastrocnemius muscle to the calcaneus. This structure is essential to everyday activities and athletic performance because it transfers force from the triceps surae (three-headed muscle in the posterior compartment of the leg) muscles to the foot and stores and releases energy during repeated and dynamic actions. The Achilles tendon is the strongest, thickest, and longest tendon in the human body. However, Achilles tendon injury is one of the most common tendon injuries in athletes and the public (Sprague et al., 2020; Schneebeli et al., 2020; Tarantino et al., 2020).

The Achilles tendon functions as a spring, storing strain energy

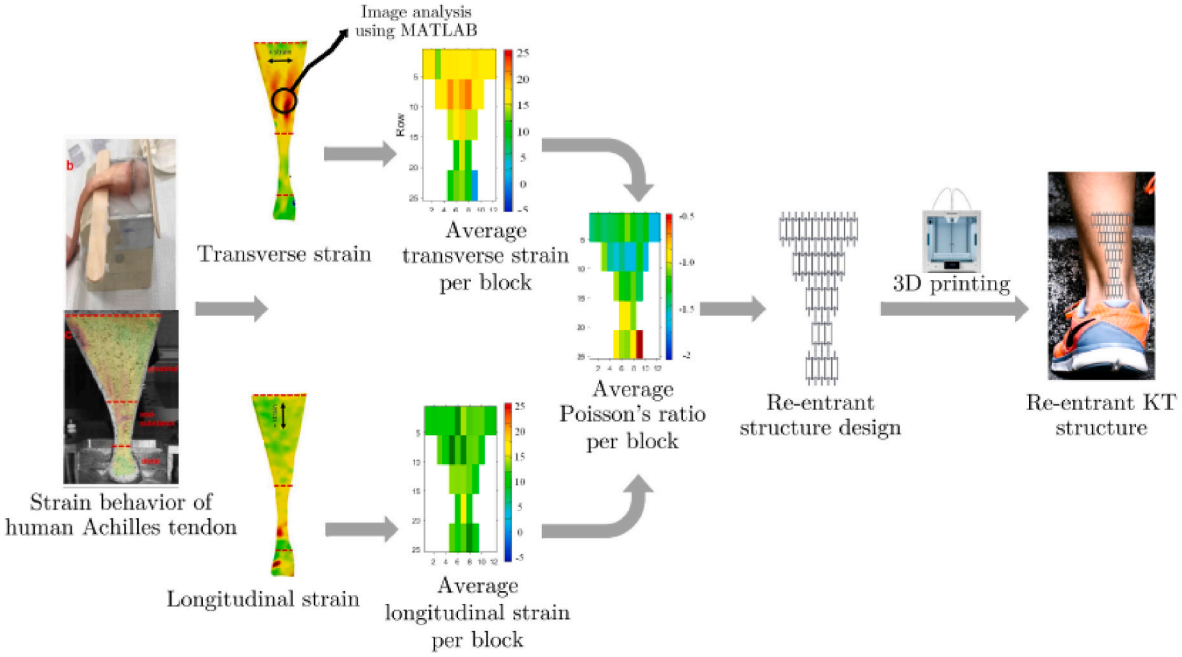

Fig. 2. The steps of analysing, designing and manufacturing of novel KT Achilles tendon.

during compression and releasing it during extension, facilitating forward movement (Yin et al., 2021). Several studies have investigated the mechanical behavior of the Achilles tendon during different activities such as walking, running, and jumping (Sprague et al., 2020; Schneebeli et al., 2020; Kharazi et al., 2021; Notermans et al., 2019; Haen et al., 2017). Investigations have revealed that the Achilles tendon has unexpected mechanical properties when the Achilles tendon is stretched, becoming thicker in cross-sectional area perpendicular to the applied load, thus showing auxetic behaviour (Gatt et al., 2015).

Several methods such as partial replacement of the tissue (Bah et al., 2020; Morais et al., 2020) are employed to treat Achilles tendon injury. One of the well-known treatments that help recover muscles after an injury and strengthen the weak muscle or tendons is using Kinesio Taping (KT) (Lee and Yoo, 2012; Huang et al., 2011; Meeusen et al., 2022b). Kenzo Kase invented these tapes in the 1970s, and they were first used by Japan's international volleyball team. KT are composed of cotton and polymer fibers (Meeusen et al., 2022b; Skirven et al., 2011). The auxetic structures, especially when designed with a graded pattern, can become very useful in designing soft implants that mimic the auxetic behavior of biological tissues.

Several studies (Hedayati et al., 2016; Gibson and Ashby, 1999; Masters and Evans, 1996) have presented analytical solutions for the mechanical behaviour of hexagonal honeycomb structures where their interior cell angle is positive (see Fig. 1b). In all previous works, the analytical solutions for simple hexagonal unit cells have been used for both honeycomb ($\theta > 0$) and 2D re-entrant structure ($\theta < 0$). The present study is dedicated to finding out whether or not the analytical solution developed for the hexagonal honeycomb structure can be used for re-entrant structures as well.

Several studies have used different strategies to design novel structures using non-uniform distribution of mechanical metamaterials. Hedayati et al. (2021a) introduced different patterns of graded distribution of re-entrant unit cells for simple tubular configurations to reach desired shape changes when subjected to the external load. Zeng et al. (2023) employed different gradient mechanical metamaterials to generate different design property requirements of microstructures using Deep Learning algorithms. Xu et al. (2023) employed the non-uniform distribution of foam-filled re-entrant unit cells to investigate the effect of some geometrical parameters, such as unit cell wall thickness on the mechanical properties of re-entrant structures. The noted research works have not employed re-entrant unit cells to design structures that can mimic the mechanical behavior of an existing tendon or structure, for instance Achilles tendon, by altering the cell interior angle only.

The present study presents an analytical solution for honeycomb/re-entrant structures where the solution is valid for the interior angles ranging from negative to positive values. The finite element method (FEM) is used to validate the developed analytical solution. Moreover, in this research, the Achilles tendon's auxetic behavior is examined using available literature, and Poisson's ratio is determined for different regions of the Achilles tendon. A novel auxetic KT with non-uniform distribution of re-entrant unit cells to match the mechanical properties (strain distributions and Poisson's ratios) of Achilles tendon is also designed and fabricated using 3D printing manufacturing technology. The distribution of auxecity in the re-entrant unit cells in KT is selected based on the strain result images obtained from the deformation of an actual Achilles tendon. The process from design to manufacturing of the novel re-entrant KT is presented in Fig. 2.

2. Materials and methods

2.1. 2D re-entrant lattice structure

2.1.1. Stiffness matrix

In order to derive the analytical relationships for elastic properties, a methodology similar to the method presented in (Hedayati et al., 2016) is used. Compared to (Hedayati et al., 2016), there are some minor differences in derivation such as the way the cells are organized and center-to-center distance. More details related to the stiffness matrix derivation are provided in the Appendix accompanying the paper.

The force-displacement relationship of the presented system (Fig. 1a) has the following form:

$$\begin{Bmatrix} Q_1 \\ Q_2 \\ Q_3 \\ Q_4 \end{Bmatrix} = \begin{bmatrix} k_{11} & k_{12} & k_{13} & k_{14} \\ k_{21} & k_{22} & k_{23} & k_{24} \\ k_{31} & k_{32} & k_{33} & k_{34} \\ k_{41} & k_{42} & k_{43} & k_{44} \end{bmatrix} \begin{Bmatrix} q_1 \\ q_2 \\ q_3 \\ q_4 \end{Bmatrix} \tag{1}$$

where Q_i stands for external force applied to a degree of freedom q_i. In order to calculate the forces, displacements, and rotations, first, the stiffness matrix elements k_{ij} must be calculated. By considering the geometries presented in Fig. 1, it can be seen that

$$s = \frac{1}{2}(W - H\tan\theta - h) \text{ and } l = \frac{H}{2\cos\theta}.$$

The force-displacement relationships using the stiffness matrix (derived in the Appendix) is

$$\begin{Bmatrix} Q_1 \\ Q_2 \\ Q_3 \\ Q_4 \end{Bmatrix} = \begin{bmatrix} \frac{2AE}{s} & -\frac{2AE_s}{s} & 0 & 0 \\ -\frac{2AE}{s} & \frac{4AE_s}{l}\sin^2\theta + \frac{48E_sI}{l^3}\cos^2\theta + \frac{2AE_s}{s} & -\frac{4AE_s}{l}sin^2\theta - \frac{48E_sI}{l^3}\cos^2\theta & \left(\frac{4AE_s}{l} - \frac{48E_sI}{l^3}\right)\cos\theta\sin\theta \\ 0 & -\frac{4AE_s}{l}sin^2\theta - \frac{48E_sI}{l^3}\cos^2\theta & \frac{48E_sI}{l^3}\cos^2\theta + \frac{4AE_s}{l}\sin^2\theta + \frac{4AE_s}{h} & \left(\frac{48E_sI}{l^3} - \frac{4AE_s}{l}\right)\cos\theta\sin\theta \\ 0 & \left(\frac{4AE_s}{l} - \frac{48E_sI}{l^3}\right)\sin\theta\cos\theta & \left(\frac{48E_sI}{l^3} - \frac{4AE_s}{l}\right)\cos\theta\sin\theta & \frac{4AE_s}{l}\cos^2\theta + \frac{48E_sI}{l^3}\sin^2\theta \end{bmatrix} \begin{Bmatrix} q_1 \\ q_2 \\ q_3 \\ q_4 \end{Bmatrix} \tag{2}$$

The force-displacement formulas for Timoshenko beam theory (TBT) can be obtained by substituting the expression $\frac{12E_sI}{l^3}$ in the Euler-Bernoulli theory (E-BT) equation by $\frac{1}{\frac{12E_sI}{l^3}+\frac{1}{2\kappa AG_s}}$ which yields

$$\begin{Bmatrix} Q_1 \\ Q_2 \\ Q_3 \\ Q_4 \end{Bmatrix} = \begin{bmatrix} \frac{2AE_s}{s} & -\frac{2AE}{s} & 0 & 0 \\ -\frac{2AE_s}{s} & \frac{4AE_s}{l}\sin^2\theta + \frac{4}{\frac{l^3}{12E_sI}+\frac{l}{2\kappa AG_s}}\cos^2\theta + \frac{2AE_s}{s} & -\frac{4AE_s}{l}\sin^2\theta - \frac{4}{\frac{l^3}{12E_sI}+\frac{l}{2\kappa AG_s}}cos^2\theta & \left(\frac{4AE_s}{l} - \frac{4}{\frac{l^3}{12E_sI}+\frac{l}{2\kappa AG_s}}\right)\cos\theta\sin\theta \\ 0 & -\frac{4AE_s}{l}\sin^2\theta - \frac{4}{\frac{l^3}{12E_sI}+\frac{l}{2\kappa AG_s}}cos^2\theta & \frac{4}{\frac{l^3}{12E_sI}+\frac{l}{2\kappa AG_s}}\cos^2\theta + \frac{4AE_s}{l}\sin^2\theta + \frac{4AE_s}{h} & \left(\frac{4}{\frac{l^3}{12E_sI}+\frac{l}{2\kappa AG_s}} - \frac{4AE_s}{l}\right)\cos\theta\sin\theta \\ 0 & \left(\frac{4AE_s}{l} - \frac{4}{\frac{l^3}{12E_sI}+\frac{l}{2\kappa AG_s}}\right)\sin\theta\cos\theta & \left(\frac{4}{\frac{l^3}{12E_sI}+\frac{l}{2\kappa AG_s}} - \frac{4AE_s}{l}\right)\cos\theta\sin\theta & \frac{4AE_s}{l}cos^2\theta + \frac{4}{\frac{l^3}{12E_sI}+\frac{l}{2\kappa AG_s}}\sin^2\theta \end{bmatrix} \begin{Bmatrix} q_1 \\ q_2 \\ q_3 \\ q_4 \end{Bmatrix} \tag{3}$$

Two elements of the external force matrix Q_2 and Q_3 which are the external forces acting on vertices B and C in the X direction that are equal to zero. Furthermore, the force applied on vertex C in the Y direction and the external force acting on vertex A are equal to $\sigma_y\, bW$ and $\sigma_x\, bH$, respectively. Therefore, the external force vector can be written as:

$$\begin{Bmatrix} Q_1 \\ Q_2 \\ Q_3 \\ Q_4 \end{Bmatrix} = \begin{Bmatrix} \sigma_x\, bH \\ 0 \\ 0 \\ \sigma_y\, bW \end{Bmatrix} \tag{4}$$

2.1.2. Mechanical properties

By inverting the stiffness matrix given in Eq. (3) and then multiplying by Eq. (4), the external force matrix, the mechanical properties can be determined. In this regard, first the q_i are determined, after which the elastic modulus, Poisson's ratio, and yield stress formulas as functions of material constants $E_s, \sigma_{y_s},$ and ν_s can be found. In all the following derivations, the formulas $s = \frac{1}{2}(W - H\tan\theta - h)$ and $l = \frac{H}{2\cos\theta}$ are considered.

a) Elastic Modulus

In order to calculate the elastic modulus, the stress (i.e. $\sigma_x\, W/\, 2q_1$ is stress in the X direction and $\sigma_y H/2q_4$ is the stress in the Y direction) is divided into the strain in that direction. By using the E-BT stiffness matrix, the relative elastic modulus in the X direction is obtained as ($\sigma_y = 0$):

$$\left(\frac{E}{E_s}\right)_X = \frac{Wt^3\, cos\,\theta}{H\left\{l(l^2-t^2)\cos^3\theta + t^2(l+W)cos\,\theta - Ht^2\, sin\,\theta\right\}} \tag{5}$$

and in the Y direction, it is obtained as:

$$\left(\frac{E}{E_s}\right)_Y = \frac{Ht^3}{Wl\left\{\left(l^2-t^2\right)sin^2\,\theta + t^2\right\}} \tag{6}$$

Moreover, by using the TBT stiffness matrix, the relative elastic modulus in the X direction is determined as:

$$\left(\frac{E}{E_s}\right)_X = \frac{5Wt^3\, cos\,\theta}{H\left\{l\left(5l^2+7t^2+11t^2\nu_s\right)\cos^3\theta + 5t^2(l+W)cos\,\theta - 5Ht^2\, sin\,\theta\right\}} \tag{7}$$

and the relative elastic modulus in the Y direction is obtained as:

$$\left(\frac{E}{E_s}\right)_Y = \frac{5Ht^3}{Wl\left\{\left(5l^2+7t^2+11t^2\nu\right)sin^2\,\theta + 5t^2\right\}} \tag{6}$$

b) Poisson's ratio

For ν_{xy}, we have $\nu_{xy} = -\frac{\varepsilon_y}{\varepsilon_x} = \frac{q_4}{q_1}\,\frac{W}{H}$ for $\sigma_y = 0$. Using the E-BT force-displacement relationship, Poisson's ratio ν_{xy} is found as

$$\nu_{xy} = \frac{Wl\, cos^2\,\theta\, sin\,\theta\left(l^2-t^2\right)}{H\left\{l\left(l^2-t^2\right)\cos^3\theta + t^2(l+W)cos\,\theta - Ht^2\, sin\,\theta\right\}} \tag{7}$$

and for TBT, it becomes

$$\nu_{xy} = \frac{Wl\, cos^2\,\theta\, sin\,\theta\left(5l^2+11\nu t^2+7t^2\right)}{H\left\{l\left(5l^2+7t^2+11t^2\nu\right)\cos^3\theta + 5t^2(l+W)cos\,\theta - 5Ht^2\, sin\,\theta\right\}} \tag{8}$$

For ν_{yx}, we have $\nu_{yx} = -\frac{\varepsilon_x}{\varepsilon_y} = \frac{q_1}{q_4}\,\frac{H}{W}$ for $\sigma_x = 0$ which for E-BT gives:

$$\nu_{yx} = \frac{H\left(l^2-t^2\right)sin(2\theta)}{2W\left\{\left(l^2-t^2\right)sin^2\,\theta + t^2\right\}} \tag{9}$$

and for TBT, it becomes

$$\nu_{yx} = \frac{H\left(5l^2+11\nu_s t^2+7t^2\right)sin(2\theta)}{W\left(11\nu_s t^2+5l^2+17t^2-\left(5l^2+7t^2+11\nu_s t^2\right)cos(2\theta)\right)} \tag{10}$$

c) Yield stress

For the honeycomb unit cell subjected to X direction loading, Y direction loading, as well as bi-axial loading, the end points of the inclines edge BC are the locations where the maximum stress occurs. If Point B is displaced for q_2 in the Y direction, and Point C is displaced for q_4 and q_3 in the X and Y directions respectively, by supposing that beam BC is clamped at one of its end points B or C, the increase in the axial length of beam BC is $q_4\sin\theta + (q_2 - q_3)\cos\theta$. Furthermore, the lateral displacement of the free end of beam BC is $(q_2 - q_3)\sin\theta - q_4\cos\theta$. Due to the noted displacements, axial load and bending moments are generated in the beam, which are equal to:

$$P = \frac{AE_s}{l}(q_4\, sin\,\theta + (q_2-q_3)cos\,\theta)\; M = \frac{6E_sI}{l^2}((q_2-q_3)sin\,\theta - q_4\, cos\,\theta) \tag{11}$$

These load and bending moments result in axial normal and flexural stresses of:

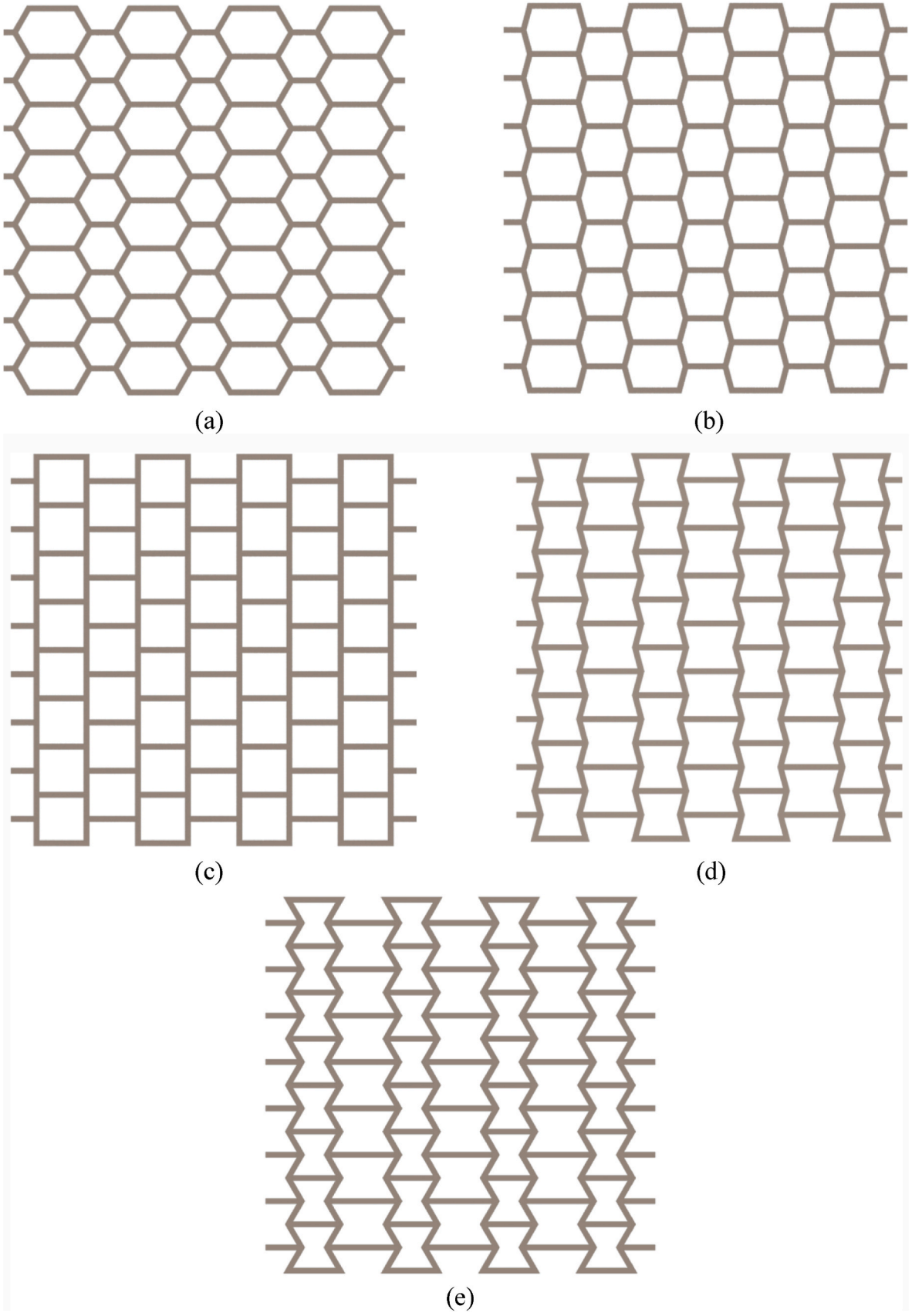

Fig. 3. 3D printed samples configuration for analytical solution validation for internal angles of (a) **30**°, (b) **15**°, (c) 0, (d) − **15**°, and (e) − **30**°.

$$\sigma_{axial}=\frac{E_s}{l}(q_4\ sin\ \theta+(q_2-q_3)cos\ \theta)\ \sigma_{flexure}=\frac{3E_s a}{l^2}((q_2-q_3)sin\ \theta-q_4\ cos\ \theta) \tag{12}$$

By adding the axial and flexural stress in the above equation, the maximum stress is $\sigma_{max}=|\sigma_{axial}|+|\sigma_{flexure}|$. Hence, the yield stress can be found by

$$\sigma_{pl}=\frac{\sigma_{ys}\sigma_i}{\sigma_{max}} \tag{13}$$

where σ_{ys} is the yield stress of the constituent material, and σ_i is the applied stress in direction i. The relative yield stress based on E-B beam theory in the X direction is found as

$$\left(\frac{\sigma_y}{\sigma_{ys}}\right)_X=\frac{2t^2}{H(3l|cos(\theta)|+t|sin(\theta)|)} \tag{14}$$

and for the TBT, it is obtained as

$$\left(\frac{\sigma_y}{\sigma_{ys}}\right)_X=\frac{10lt^2}{H\left(3\left|\left(11\nu_s t^2+5l^2+12t^2\right)cos(\theta)\right|+5lt|sin(\theta)|\right)} \tag{15}$$

The relative yield stress in the Y direction and for E-B beam theory is calculated as:

$$\left(\frac{\sigma_y}{\sigma_{ys}}\right)_Y=\frac{2t^2}{W(t|cos(\theta)|+3l|sin(\theta)|)} \tag{16}$$

and for the TBT, it is obtained as

$$\left(\frac{\sigma_y}{\sigma_{ys}}\right)_Y=\frac{10lt^2}{W\left(5lt|cos(\theta)|+3\left|\left(11\nu_s t^2+5l^2+12t^2\right)sin(\theta)\right|\right)} \tag{17}$$

2.1.3. Numerical modeling

By employing Finite Element Method (FEM), the derived analytical solution are evaluated and validated. To this aim, a single 2D re-entrant unit cell with periodic boundary was considered. In order to determine the mechanical properties of the 2D re-entrant unit cell by FEM, two distinct loading conditions were applied to the unit cell horizontally and vertically. As for the structure discretization, two main considerations were taken into account to gain more accurate results. First, elements based on TBT were used for descritizing the walls. Second, each beam was divided into five elements. Compared to E-BT, the TBM considers the transverse shear deformation, which leads to a better deformation prediction, especially in thick walls. The material properties of $E_s=200$ GPa and $\nu_s=0.4$ were considered for the elastic properties of the constituent material, as the bulk material has a small influence on the normalized material properties of the lattice structure. To obtain the nuemrical results for various values of θ, an APDL script was developed to reduce the analysis cost time.

It is worth mentioning that one of the unit cell nodes was kept totally constrained to prevent rigid body motion. Since the unit cells were assumed to be firmly connected at the structure's vertices, their exterior sides were also rotationally restricted. The dimensions considered for the 2D re-entrant unit cell were $W=14$ mm, $H=6.67$ mm, $b=4$ mm, and $t=0.8$ mm.

2.1.4. Experimental tests

Five types of specimens were manufactured using a Cura Ender 3 3D printer and tested under compressive loading. The specimens had five different internal angles of $-30°$, $-15°$, $0°$, $15°$, and $30°$ (Fig. 3). All the specimens had the dimensions of $W=14$ mm, $H=6.67$ mm, $b=4$ mm, and $t=0.8$ mm. A displacement rate of 2 mm/min was applied to all the specimens. The elastic modulus was obtained by measuring the gradient of the stress-strain curves in the first regime.

2.2. Achilles tendon model

2.2.1. Design

Nagelli et al. (2022) studied 11 Achilles tendons, of which 5 were female and 6 were male. All Achilles tendons had no history of injury or any surgery. Achilles tendons were loaded until failure, and digital image correlation (DIC) was used to analyze the strain behavior of all tendons at each specific percent failure load. The transverse and longitudinal strains right before failure are presented in Fig. 4. The Achilles tendon can be divided into three main regions: proximal, mid-substance, and distal (Fig. 4a). The failure usually occurs in Region 2, known as mid-substance.

In this study, Poisson's ratio at each point of the tendon was obtained using $\nu_{xy}=-\frac{\varepsilon_{transverse}}{\varepsilon_{longitudinal}}$. In order to evaluate the value of transverse and longitudinal strains, a MATLAB code was developed, which, based on the color bar presented in Fig. 4b, assigned a specific strain value to each pixel of the Achilles tendon (ranging from −5 to 25). Afterward, based on the selected re-entrant unit cell dimensions ($W=0.03414$ m, $H=$

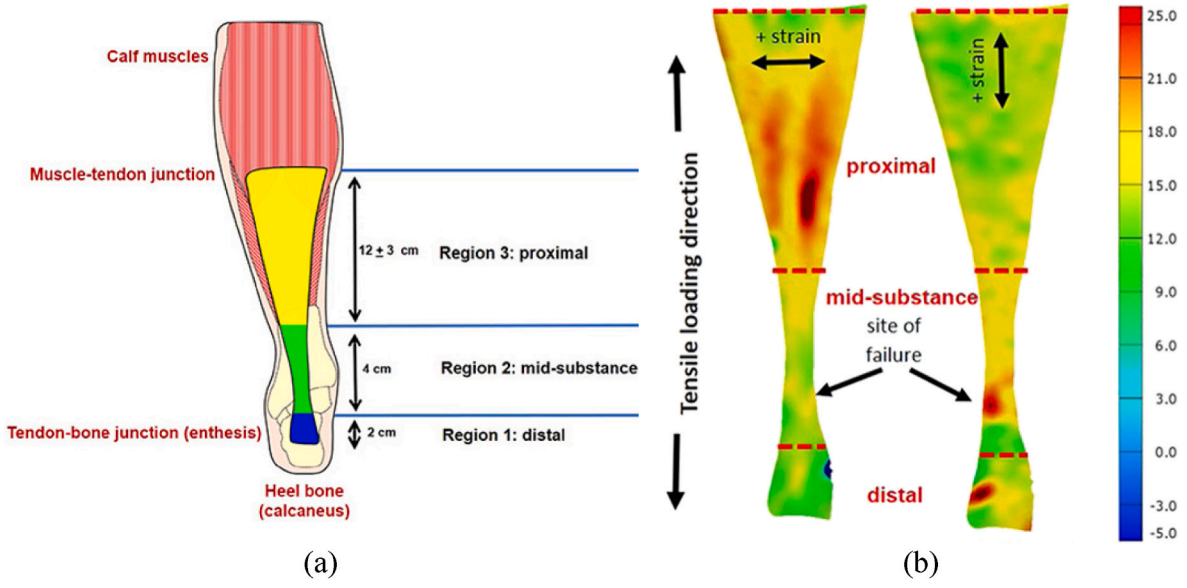

Fig. 4. (a) Achilles tendon sections and dimensions. (b) Transverse strain (left) and longitudinal strain (right) contours right before final rupture (Nagelli et al., 2022).

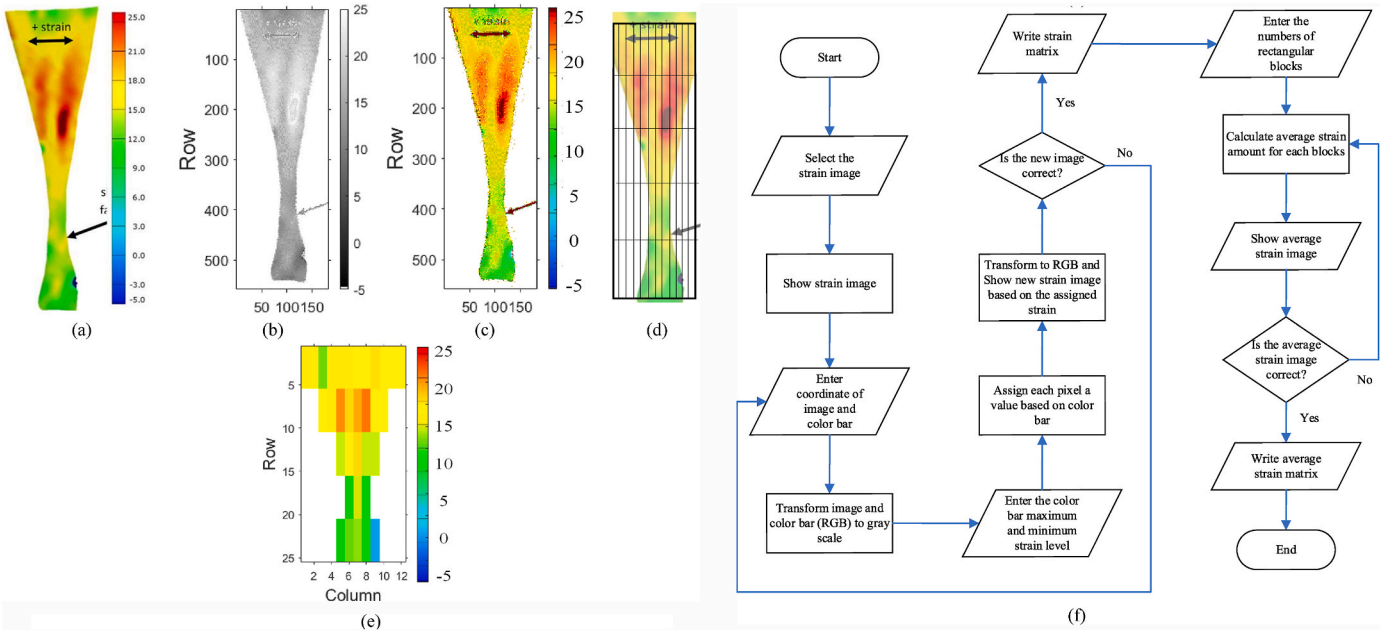

Fig. 5. Different steps of transverse strain averaging in Achilles tendon: (a) Achilles tendon transverse strain, (b) grayscale contour of Achilles tendon transverse strain, (c) exported color image of MATLAB code analysis, (d) unit cell block positioning based on the form of Achilles tendon, (e) average value of transverse strain in each cell, and (f) MATLAB code flow chart.

0.0061 m, and $t = 0.0008$ m), the Achilles tendon was divided into 5 rows longitudinally. The number of columns in each row depended on the width of the Achilles tendon at each region. For instance, 12 columns were considered for the proximal region's top part, while three columns were considered for the narrower section in the mid-substance region. Finally, in each row, the average amount of strain was calculated.

Fig. 5a–e demonstrates the procedure in more detail. First, MATLAB reads the image and color bar (Fig. 5a), after which it crops the strain contour image and the color bar image separately. Then, both the strain contour image and color bar image are transformed into grayscale images in MATLAB (Fig. 5b). In this stage, the maximum and minimum strain levels are determined by MATLAB code based on the color bar image. In the next step, MATLAB assigns each pixel a strain value based on the grayscale pixel value and transforms it into a colorful image to ensure that the code is viable (Fig. 5c). Afterward, based on the dimensions of each re-entrant unit cell and the geometrical form of the Achilles tendon, the plane is discretized into some regions of rectangular blocks (Fig. 5d). Finally, the average amount of transverse strain for each rectangle is calculated (Fig. 5e). The flow chart of the developed MATLAB code is presented in Fig. 5f.

For calculating longitudinal strain (Fig. 6), the same procedure as the one described for the transverse strain was performed (Fig. 5). As illustrated in Fig. 6d, only sections were considered for constructing unit cells in the FE model that the Achilles tendon could almost cover the considered rectangle if they were to be put on top of each other (Fig. 7a).

Fig. 7a shows the KT design made up of unit cells which were constructed based on the dimensions of the unit cells as well as the geometry of the considered Achilles tendon. After calculating both average transverse and longitudinal stains, the average Poisson's ratio at each section was determined, and it is indicated in Fig. 7.

Ensuing determining the Poisson's ratio in the Achilles tendon, the Kinesio Taping was designed. In this regard, each unit cell was selected based on the corresponding rectangle's Poisson's ratio in Fig. 7b. Using the dependency of the re-entrant angle vs. Poisson's ratio, the Poisson's ratio values presented in Fig. 7b were transformed into a relevant re-entrant's angle for the KT design (see Fig. 8a). The initial design based on the determined angles is presented in Fig. 8b. According to Fig. 7b, the Poisson's ratio in the Achilles tendon ranges from − 0.5 to − 2. Therefore, the re-entrant design should generate Poisson's ratio levels in the range of −0.5 and −2 by changing the unit cell internal angle. According to the open literature (Ling et al., 2020), the re-entrant designs with $\frac{W}{H} \geq 4$ are capable of generating this range of Poisson's ratio in large deformation regime. Moreover, as the length of the Achilles tendon is higher than the width, particularly in the midpart region, in order to use sufficient number of unit cells in this section, H must be selected to be as small as possible. The width of Achilles tendon is almost 0.0183 m in this section, so H is considered to be 0.0061 m leading to 3 unit cells in the width of this region. Therefore, as mentioned earlier, the dimensions of $W = 0.03414$ m, $H = 0.0061$ m, and $t = 0.0008$ m were selected for the re-entrant unit cell.

As the materials used for printing KT was thermoplastic polyurethane (TPU), numerical modeling was used to relate the re-entrant angles and Poisson's ratio in large deformations, the results of which can be found in Table 1. For each angle (θ), a lattice structure that had 5 rows and 10 columns was loaded axially, and by calculating the transverse and longitudinal strain, the Poisson's ratio was determined. The Poisson's ratio of Achilles tendon ranges from −0.5 to − 2, meaning that the re-entrant design must be able to generate Poisson's ratio close to the noted range. Therefore, the internal angle was varied from −35° to −60° in the design to generate Poisson's ratio close to the Poisson's ratio of Achilles. Both the right and left edges of the structures demonstrated in Table 1 were restricted in the Y direction. Moreover, the left edges of the structures were restricted in the X direction, and a horizontal stroke of 10 mm was applied to the right edge of each structure.

2.2.2. Experimental setup

Due to its capability to manufacture highly complex shapes, additive manufacturing has gained popularity in tissue engineering recently (Warner et al., 2017; Wanniarachchi et al., 2022; Shirzad et al., 2021). The auxetic re-entrant Achilles tendon structure was printed using the fused deposition modeling (FDM) technique. An Ultimaker S3 3D printer (Netherlands) was implemented, and the TPU (Filaflex 60A, Recreus, Spain) was chosen as the material. The printing layer height was set to 0.15 mm, and a working temperature of 215 °C was chosen for the nozzle, while the build platform and chamber temperatures were kept at 25 °C. The print head speed was set to 20 mms^{-1}, and the thickness of

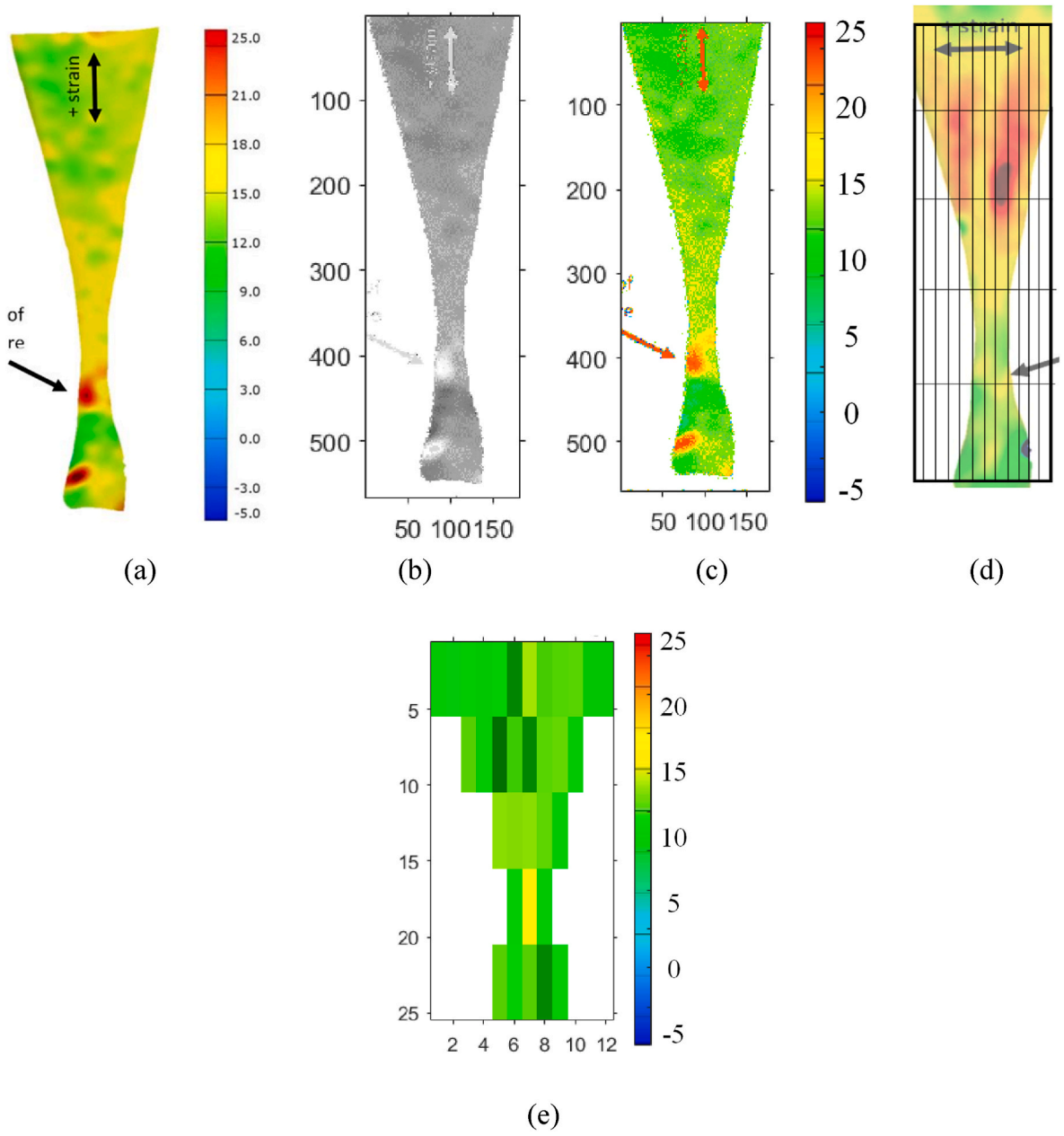

Fig. 6. Different steps of longitudinal strain averaging in Achilles tendon: (a) Achilles tendon longitudinal strain, (b) grayscale contour of Achilles tendon longitudinal strain, (c) exported color image of MATLAB code analysis, (d) unit cell block positioning based on the form of Achilles tendon, and (e) average value of longitudinal strain in each cell.

cell walls was 0.8 mm.

In the next step, to determine the mechanical properties of TPU material, according to ASTM D638 standard (Standard, 2010), dog-bone specimens (type IV) with a thickness of 3 mm were printed. Three dog-bone specimens were printed, and the tensile test was carried out by employing Tinius Olsen® H5kS (Tinius Olsen, Horsham, PA, USA) equipped with a 5 kN load cell. The 3D-printed re-entrant auxetic Achilles model is illustrated in Fig. 9a. The average stress-strain curve for the TPU dog-bone specimens is presented in Fig. 9b.

2.2.3. Numerical modeling

SOLIDWORKS (Dassault Systèmes, France) was used to design the geometry of the re-entrant KT structure. Afterward, the SOLIDWORKS Application file (.x_t) was exported to the ABAQUS software package (V.6.14, Dassault Systems, France). In order to model TPU based on the stress-strain curve, the Mooney-Rivlin hyperelastic model was considered. The Mooney–Rivlin constants were determined using Evaluate Materials option in ABAQUS ($C_{10} = 0.195\ MPa$; $C_{01} = 0.232\ MPa$; $D_1 = 0.558\ MPa^{-1}$). Subsequently, the dynamic implicit quasi-static solver was used for solving the FE model. The lower side of the structure was fixed entirely in both the *X* and *Z* directions (Fig. 10a). A displacement of 6.9 mm (i.e. a global strain of 4%) was applied on the upper side of the structure, and it was fixed in the *Z* direction. According to Kharazi et al. (2021), the peak strain value during walking is around 4%; hence the strain applied to the re-entrant KT structure is close to strain levels the tendon experiences in real life. Linear tetrahedral elements of type C3D4H were utilized to discretize the structure (Fig. 10b). Mesh sensitivity analysis was performed to ensure the accuracy of the results (Table 2), and an element size of 0.4 mm was found to be suitable considering both accuracy and computational time.

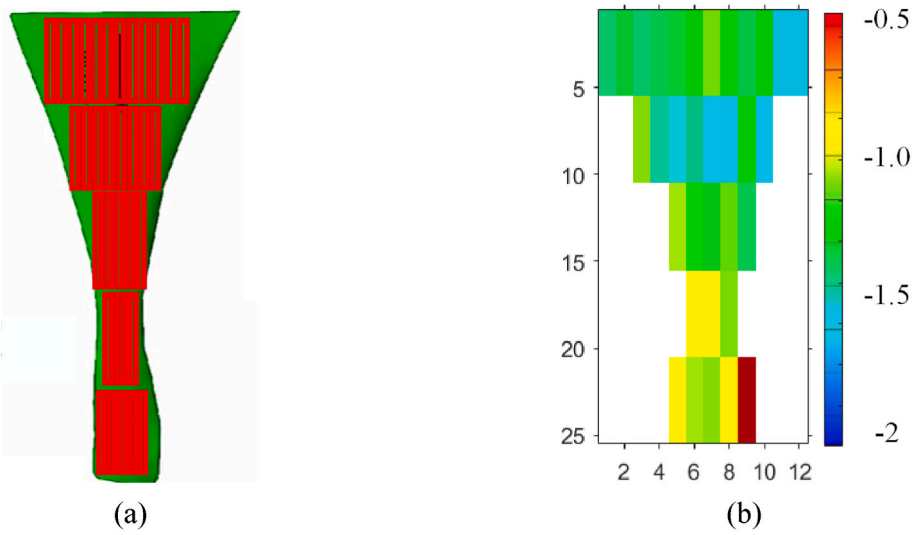

Fig. 7. (a) Arrangement of re-entrant unit cells, and (b) average Poisson's ratio distribution of Achilles tendon.

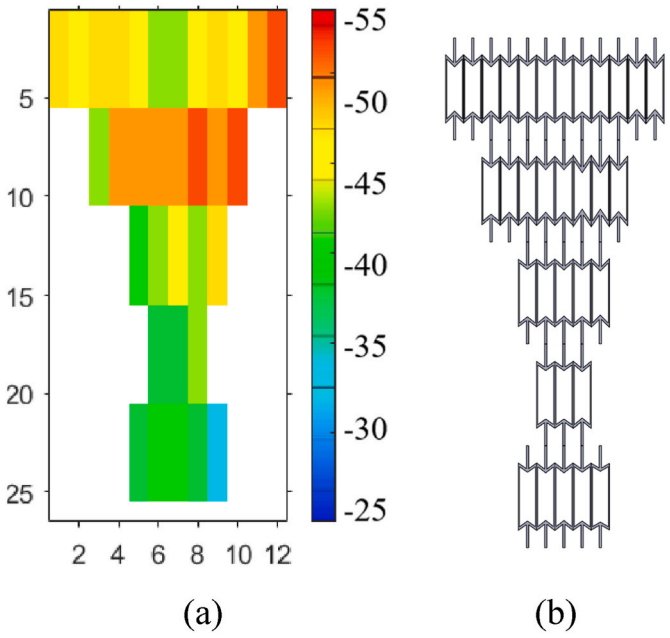

Fig. 8. (a) Re-entrant's angles distribution, (b) initial KT structure.

3. Results and discussions

3.1. 2D re-entrant lattice structure

First, the analytical results of the present research are compared to the findings of the prior studies (Hedayati et al., 2016; Gibson and Ashby, 1999; Masters and Evans, 1996), which entails taking $s = h/2$, since the previous studies have considered this ratio. The elastic modulus analytical values obtained in this research were found to be greater than the analytical values obtained from Masters and Evans's analytical model (Masters and Evans, 1996), while they were lower than the values obtained based on relationships presented by Gibson and Ashby (Gibson and Ashby, 1999) and Hedayati et al. (Hedayati et al., 2016) (see Fig. 11a and b). While the E_x curves had a domical shape, the E_y curves were bell-shaped. Overall, the results presented here are relatively close to those of Masters and Evans (1996) and Hedayati et al. (2016), while the reported results have significant differences with Gibson and Ashby's results (Gibson and Ashby, 1999), see Fig. 11a and b. Gibson and Ashby's analytical solution (Gibson and Ashby, 1999) reported infinite value for E_y at $\theta = 0$ (Fig. 11b) which cannot be physically true. In Hedayati et al. study (Hedayati et al., 2016), it was shown that Gibson and Ashby's (Gibson and Ashby, 1999) formulations are only applicable to very thin (metal sheet) honeycombs due to several simplifying assumptions they have made in their derivations. Therefore, for additive manufactured honeycombs that are thick due to manufacturing limitations, Gibson and Ashby's (Gibson and Ashby, 1999) analytical solution deviates from the experimental and numerical results.

Except for Gibson and Ashby's (Gibson and Ashby, 1999) formulations, all Poisson's ratio curves (Fig. 11c–d) exhibited excellent overlap with one another. When θ approached zero, Gibson and Ashby's (Gibson and Ashby, 1999) formulations produced non-realistic extreme values for ν_{yx}. It is worth mentioning that all curves had symmetry with respect to the origin of the plot (i.e. $\theta = 0$ and $\nu = 0$).

Next, the yield strength results are presented and compared to those available in previous studies. It is worth noting that other studies were not able to give accurate yield stress results for $\theta < 0$ (curves are presented by dashed grey curves in Fig. 11e–f). It must be noted that, the results for negative ranges of θ are reported here for other studies although those studies have not necessarily claimed that their derived analytical solutions are also applicable for $\theta < 0$.

The yield strength results of the developed analytical model showed good agreement with numerical results for a wide range of internal angel (for both $\theta < 0$ and $\theta > 0$). The yield stress values were symmetrical with respect to the line $\theta = 0$ (Fig. 11e–f). It is worth mentioning that the yield stress curves in the X direction were almost independent of θ, while in the Y direction, a peak point could be observed in the curve.

Fig. 11 shows that the proposed analytical solution is the most accurate among all the analytical solution available in the literature. It is worth mentioning that the reported results in Fig. 11 are plotted for $\frac{s}{h} = 1/2$, since this ratio is considered in the previous studies (Hedayati et al., 2016; Gibson and Ashby, 1999; Masters and Evans, 1996). For most mechanical metamaterials, including gradient (Hedayati et al., 2018) and random (Mirzaali et al., 2017) metamaterials, to have the same width W and height H for all the unit cells in the lattice structure, the ratio s/h must change. See for example the unit cells presented in Fig. 1b and c, which have the same width W and height H. Fig. 12 presents the mechanical properties of the unit cell with variable s/h.

By comparing the results of Fig. 11 (constant s/h) and Fig. 12 (variable s/h), it can be seen that elastic modulus graphs for the case of

Table 1
The relation between re-entrant angle and Poisson's ratio.

θ	X displacement	Y displacement	ν
$\theta = -60^{\circ}$	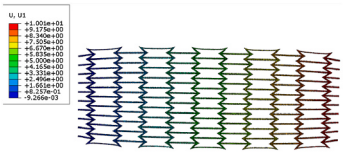 $d_{max} = 10\ mm \rightarrow \varepsilon =$ 5.84%	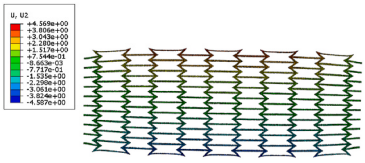 $d_{max} = 9.16\ mm \rightarrow \varepsilon =$ 15.01%	$\nu = -2.57$
$\theta = -55^{\circ}$	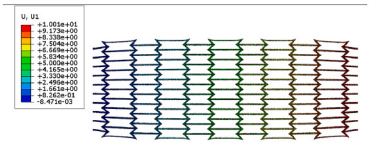 $d_{max} = 10\ mm \rightarrow \varepsilon =$ 5.84%	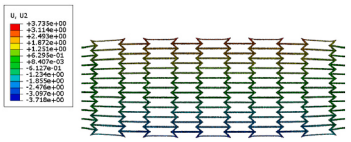 $d_{max} = 7.45\ mm \rightarrow \varepsilon =$ 12.21	$\nu = -2.09$
$\theta = -50^{\circ}$	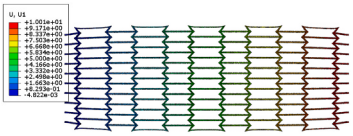 $d_{max} = 10\ mm \rightarrow \varepsilon =$ 5.84%	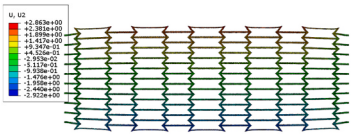 $d_{max} = 5.78\ mm \rightarrow \varepsilon = 9.47$	$\nu = -1.67$
$\theta = -45^{\circ}$	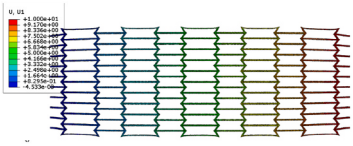 $d_{max} = 10\ mm \rightarrow \varepsilon =$ 5.84%	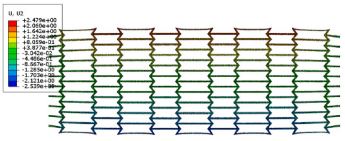 $d_{max} = 5.02\ mm \rightarrow \varepsilon = 8.23$	$\nu = -1.41$
$\theta = -40^{\circ}$	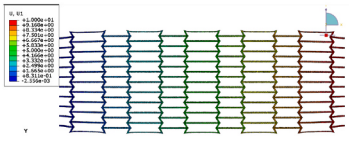 $d_{max} = 10\ mm \rightarrow \varepsilon =$ 5.84%	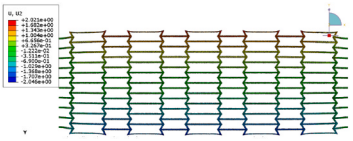 $d_{max} = 4.07\ mm \rightarrow \varepsilon =$ 6.67%	$\nu = 1.14$
$\theta = -35^{\circ}$	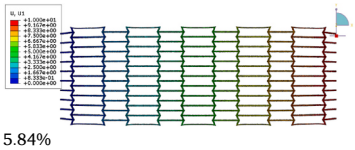 $d_{max} = 10\ mm \rightarrow \varepsilon =$ 5.84%	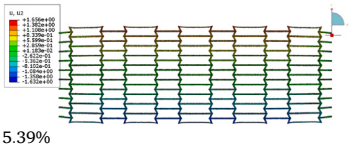 $d_{max} = 3.29\ mm \rightarrow \varepsilon =$ 5.39%	$\nu = -0.92$

variable s/h are slightly lower than that of constant $s/\ h$ (with a maximum difference of 0.59% in the X direction and 0.38% in the Y direction). Poisson's ratio values for lattice structures with variable $s/\ h$ are also slightly lower than the corresponding values for lattice structures with constant s/h (with a maximum difference of 0.077% for xy and 0.036% for yx). Nonetheless, the yield stress values were almost identical.

3.2. Tendon

This section presents the results obtained from the re-entrant KT structure. It is worth mentioning that our main aim was to mimic the deformation of the Achilles tendon as much as possible by distributing the angle of the unit cells nonuniformly throughout the lattice structure. To reach this goal, the local Poisson's ratio of the designed KT and Achilles tendon must be very close. The Poisson's ratio of each row of the KT design was calculated by measuring the longitudinal and lateral displacements of each row. The results were compared to the side-by-side Poisson's ratio of the corresponding height of the Achilles tendon under experimental tests (Nagelli et al., 2022).

The deformation as well as longitudinal and transverse displacement contours of the initially developed re-entrant KT structure is presented in Fig. 13. The variations of experimental (Achilles tendon) and numerical Poisson's ratio along the height of the Achilles tendon are compared in Fig. 14. It can be seen that there are considerable differences between the Poisson's ratio of the initially designed re-entrant KT structure and the Achilles tendon, especially in the mid part of the tendon. This can be attributed to the stress path through the KT design, which passes mostly through the tendon's middle axial region, leading to expected levels of Poisson's ratio in the central axis of the KT design but much lower magnitudes of the Poisson's ratio in the side parts of the tendon. In order to improve the result of the KT model, the cells through which most stress flow was observed were identified using FEM. Eight impactful cells were identified in the midst of the design and they were substituted with 8 other cells with higher Poisson's ratio levels.

Therefore, some modifications were made to improve the design. Eight cells in the midst of the KT model (Fig. 15a) were replaced by re-entrant unit cells with higher re-entrant angles, i.e., 60°, resulting in a higher negative Poisson's ratio for some parts of the model. Fig. 15b presents the improved re-entrant KT design. Except for the 8 cells, all the other unit cells were kept the same as those in the initial design. The transverse and longitudinal displacement of the improved structure subjected to a global strain of 4% are presented in Fig. 15c–d. The experimental and numerical Poisson's ratio values are compared in Fig. 15e. The difference between the experimental and numerical Poisson's ratio of the improved design is less than 10% which shows the accuracy of the FE modelling. Moreover, the results show a huge improvement in the proximity of the Poisson's ratio of the improved KT

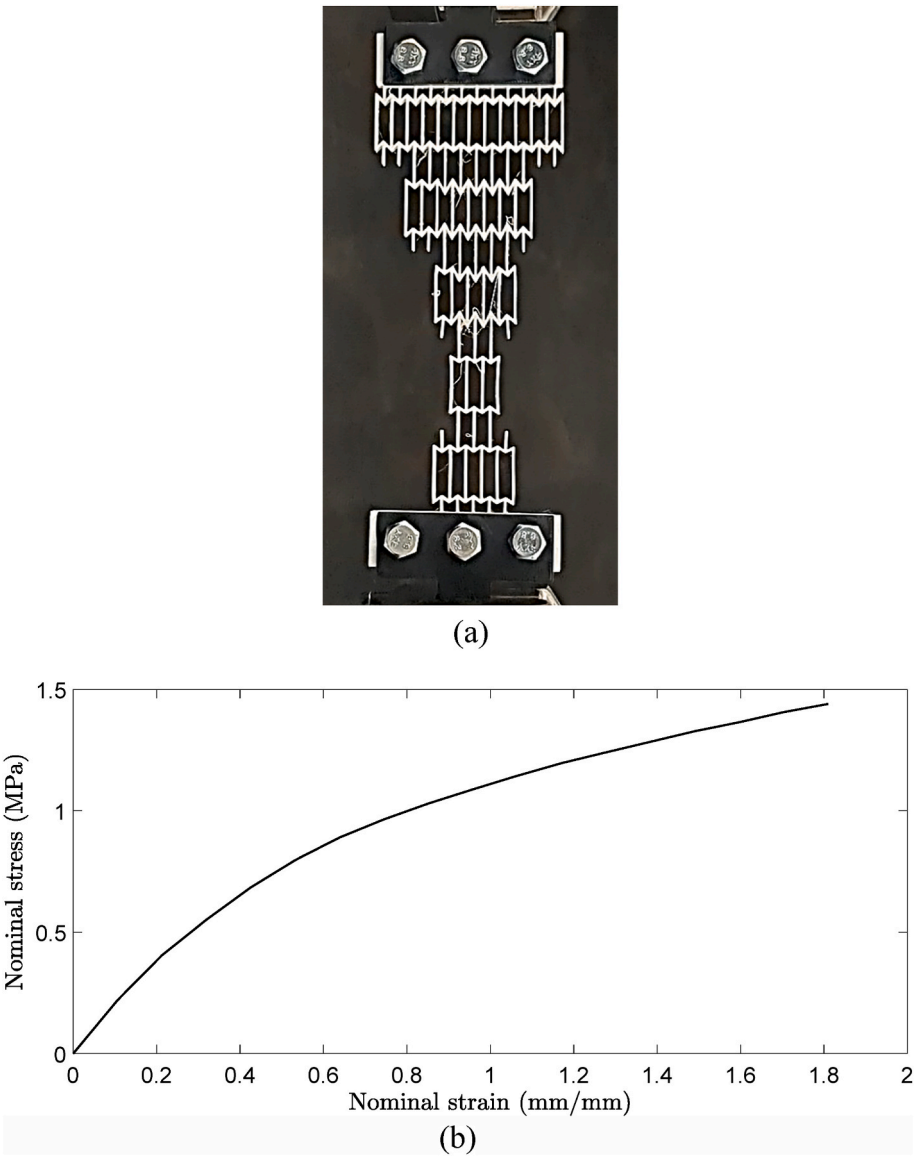

Fig. 9. (a) The 3D printed re-entrant auxetic Achilles model, (b) stress-strain curve of TPU material.

design and that of the actual Achilles tendon. The maximum difference between the Poisson's ratio of the Achilles tendon and the re-entrant KT design was <25%. Moreover, the noted difference for the first three rows was insignificant. Therefore, the improved design can model the Achilles tendon deformation efficiently.

The results for small strains, i.e., 0.2%, are also presented in Fig. 16. As can be seen, the absolute value of Poisson's ratio for improved design is increased for a loading strain of 0.2% (Fig. 16c) compared to a loading strain of 4% (Fig. 15e).

Fig. 17a and b compare the deformation of the FE model and the deformation of its manufactured counterpart. As can be seen in Fig. 17, the results of the numerical model and the manufactured specimen are very similar.

4. Discussions

4.1. Analytical solution

In previous studies, analytical solutions have been derived for several different regimes, material types, and similar re-entrant shapes. In the work of Veisi and Farrokhabadi (2021), classical laminate theory (CLT) has been used to study the mechanical response of multi-layered composite lattice structures. In the work done by Hu et al. (2018), analytical solutions for large deformation in the 2D-reentrant structures is presented. They have neglected bending in the cell walls, and their analysis is based on an elastic, perfectly plastic material behaviour which leads to plastic hinges in the corners. In work performed by Baran and Öztürk (2020), analytical relationships are presented for a modified unit cell shape with added inclined cell walls leading to an increase in the rigidity of the structure. The work by Lu et al. (2016) is based on the Euler-Bernoulli beam theory and ignores the shear deformation and rotational bending effects. Other similar works, such as (Zeng et al., 2023; Xu et al., 2023), also exist in the literature. Nonetheless, an analytical model which is capable of successfully predicting all the elastic mechanical properties (yield stress, elastic modulus, and Poisson's ratio) of a simple hexagonal unit cell in both the positive and negative ranges of the unit cell interior angle was lacking from the literature before this study. The analytical relationships presented here successfully predicted the elastic mechanical properties in both the positive and negative ranges of the unit cell interior angle.

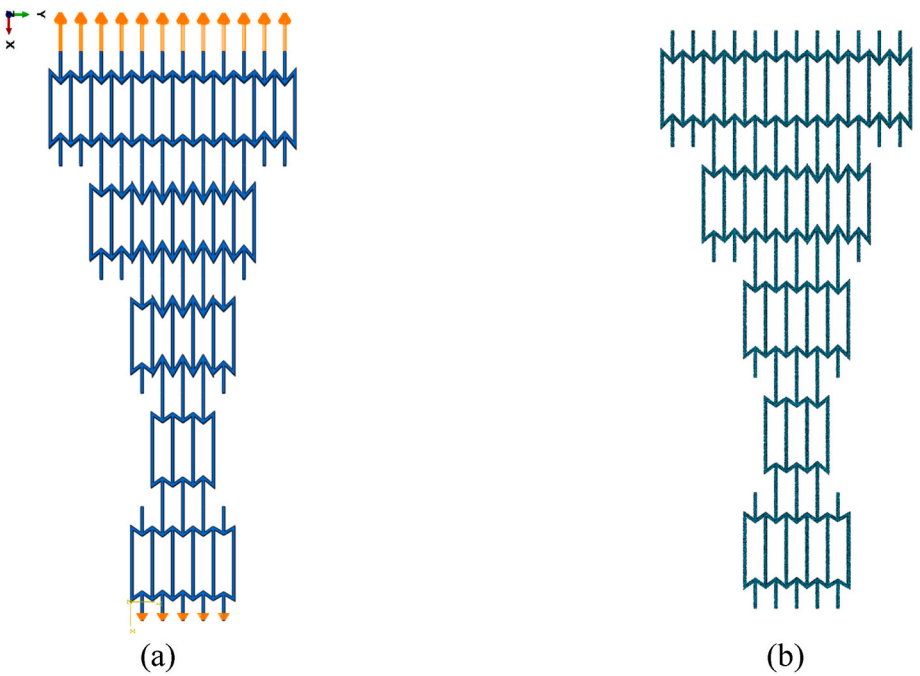

Fig. 10. (a) Loads and boundary conditions on Achilles structure and (b) a typical meshed Achilles structure.

Table 2
Mesh refinement results for the initial design.

Element size (mm)	Poisson's ratio at the first row	Poisson's ratio at the second row
1	−0.72	−1.24
0.6	−0.64	−0.90
0.4	−0.59	−0.84
0.3	−0.59	−0.84

4.2. Strain range

The present section discusses the effect of loading strain on the re-entrant structure's Poisson's ratio. According to the open literature (Ling et al., 2020; Dong et al., 2019; Fozdar et al., 2011; Ohtaki et al., 2004), in small strains (strains in the range of 0–1%), the Poisson's ratio is highly affected by the extent of loading strain. In fact, by applying smaller external strains, the absolute value of Poisson's ratio is increased. For instance, it has been reported that by reducing the loading strain from 1% to 0.5%, the absolute value of Poisson's ratio is increased by ~13% (Ling et al., 2020). Nonetheless, in the large deformation regime, the effect of loading strain on Poisson's ratio is insignificant. The results of our study showed similar behavior for the designed KT structure, and we could see a decrease of maximally 28.03% in the absolute value of Poisson's ratio for a loading strain of 4% as compared to that for the loading strain of 0.2%.

Interestingly, the Poisson's ratio of Achilles tendon also has strain-dependent behavior. In the lower loading strain, the Poisson's ratio of Achilles tendon is lower (Nagelli et al., 2021, 2022) (in other words, the absolute value of Achilles tendon Poisson's ratio is higher) than the Poisson's ratio in higher loading strains. Therefore, the present design shows very similar behavior to that of the Achilles tendon and shows that the KT design can be implemented in both small (in resting regime) and large deformations (walking regime).

It must be added that the stain contours of the designed lattice structure under a global applied strain of 4% showed that local strain levels do not exceed ~ 1%. This is due to the bending of the cell walls, which eases local strain levels. Therefore, although the global strain during walking can reach up to 4%, the local strain does not exceed a small deformation regime. Hence, the analytical solutions that are derived for small strain regimes can successfully be used for large global strains.

4.3. Application as KT

As discussed previously, one of the main applications of the re-entrant Achilles tendon-like structure is to be employed as a KT structure. According to a study in 2017, KT increases the blood flow in the skin. Using KT structures can also improve lymphatic fluid circulation, which contains mostly water, and proteins, regulating swelling (Craighead et al., 2017). The most important feature of the proposed re-entrant KT structure is duplicating the Achilles tendon's unexpected auxetic behavior. This feature of the re-entrant KT structure helps it to completely attach to the skin over the Achilles tendon. It is worth mentioning that in the present study, only the geometry of the KT design is considered and 3D printed. The manufactured KT design must also be capable of adequately attaching to the skin. In order to finalize KT product, by using the laser cutting process, a woven tape can be cut and attached to re-entrant auxetic KT structure, as discussed by Meeusen et al. (2022b).

In addition to Achilles tendon, the KT tapes with non-uniform distribution of auxetic cells can be used in several other parts of the body, such as elbows, knees, arms, etc. For instance, patients suffering from elbow pain, known as dull pain resulting from joint weakness, can use re-entrant structures to reduce the tape/skin deformation incompatibility (Meeusen et al., 2022a). The auxetic KT structure can also be designed for knee and shoulder joints, two other body parts with a lot of non-uniform deformations, to reduce the chance of joint irritation (Lyman et al., 2017).

4.4. Applications as patches, wearable devices, and on-skin sensors

Another possible application of the proposed design procedure is to use auxetic sticky patches for damaged Achilles tendons to speed up the recovery of Achilles after the rupture. Chansoria et al. (2022) developed a new type of ultra-elastic (hyper-elastic) auxetic patch that is easy to apply. These patches can be applied to a wide range of organs and tissues. Similarly, the structure presented here could be used as a patch for

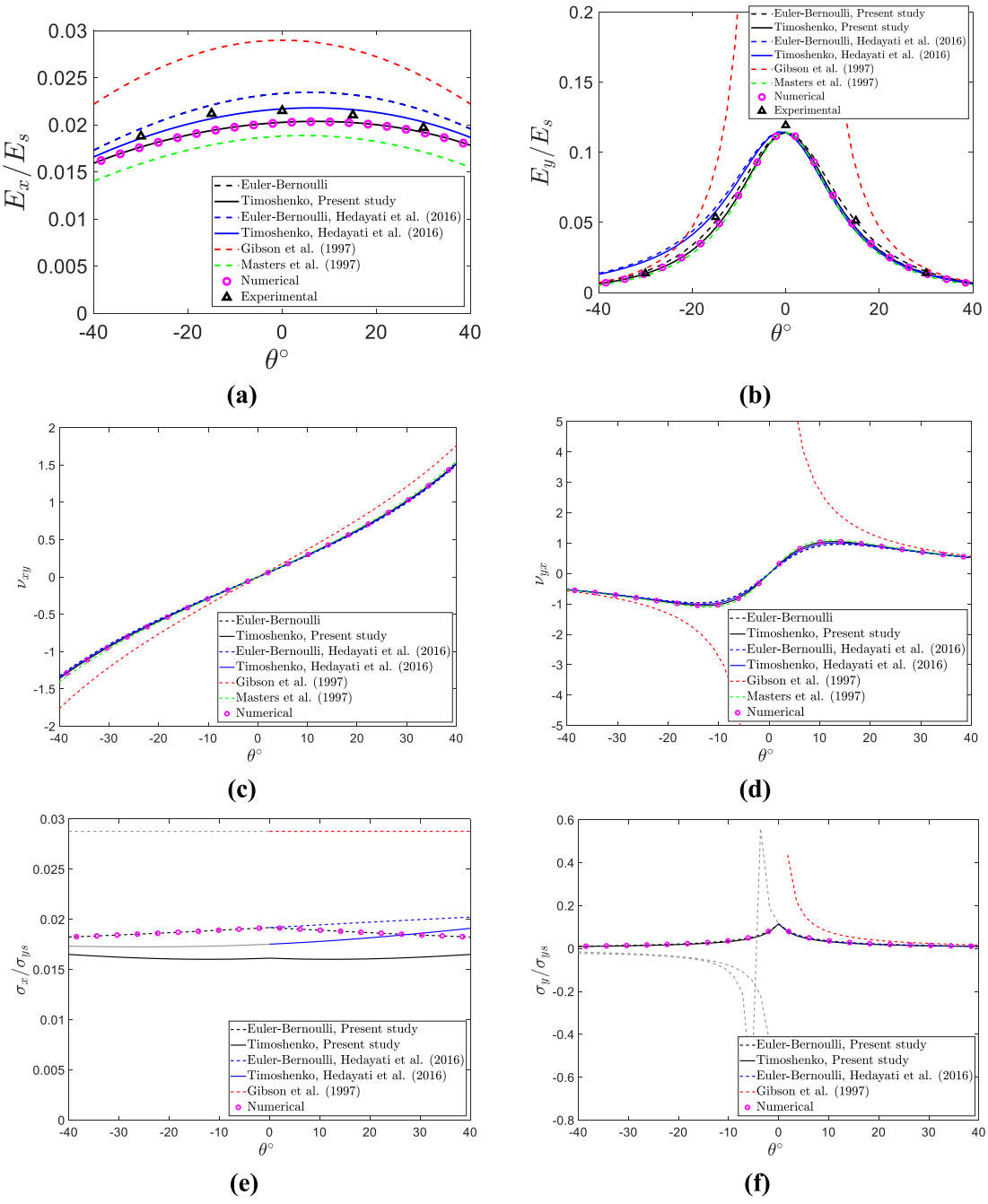

Fig. 11. Comparison between current results for (a) E_x, (b) E_y, (c) υ_{xy}, (d) υ_{yx}, (e) σ_x, and (f) σ_y and the results of previous studies for $s = h/2$. The extension of the curves attributing to the works of Hedayati et al. (Hedayati et al., 2016) and Gibson et al. (Gibson and Ashby, 1999) are presented by grey lines for $\theta < 0$.

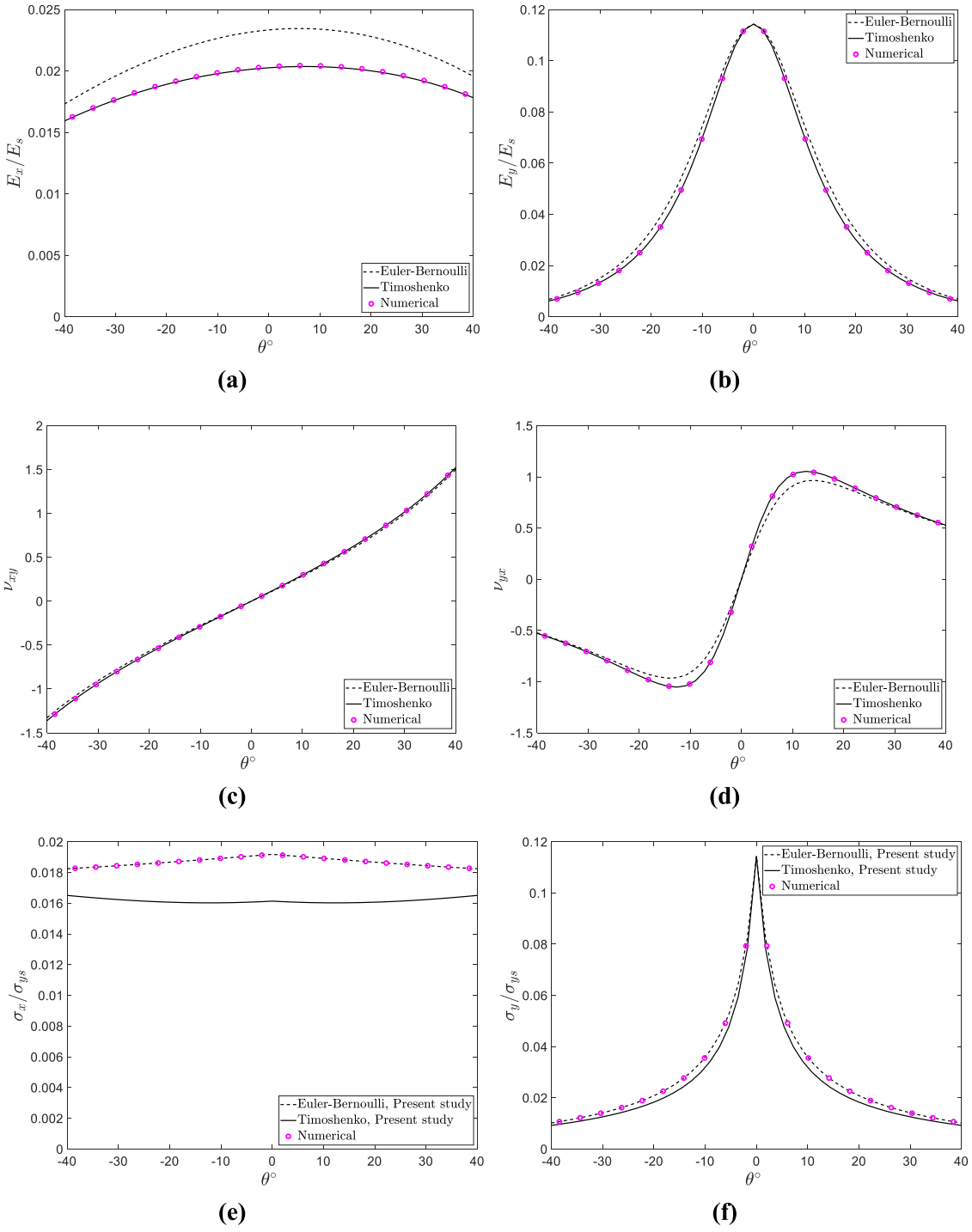

Fig. 12. Comparison of analytical and numerical results for (a) E_x, (b) E_y, (c) υ_{xy}, (d) υ_{yx}, (e) σ_x, and (f) σ_y for $s = \frac{W-Htan(\theta)-h}{2}$.

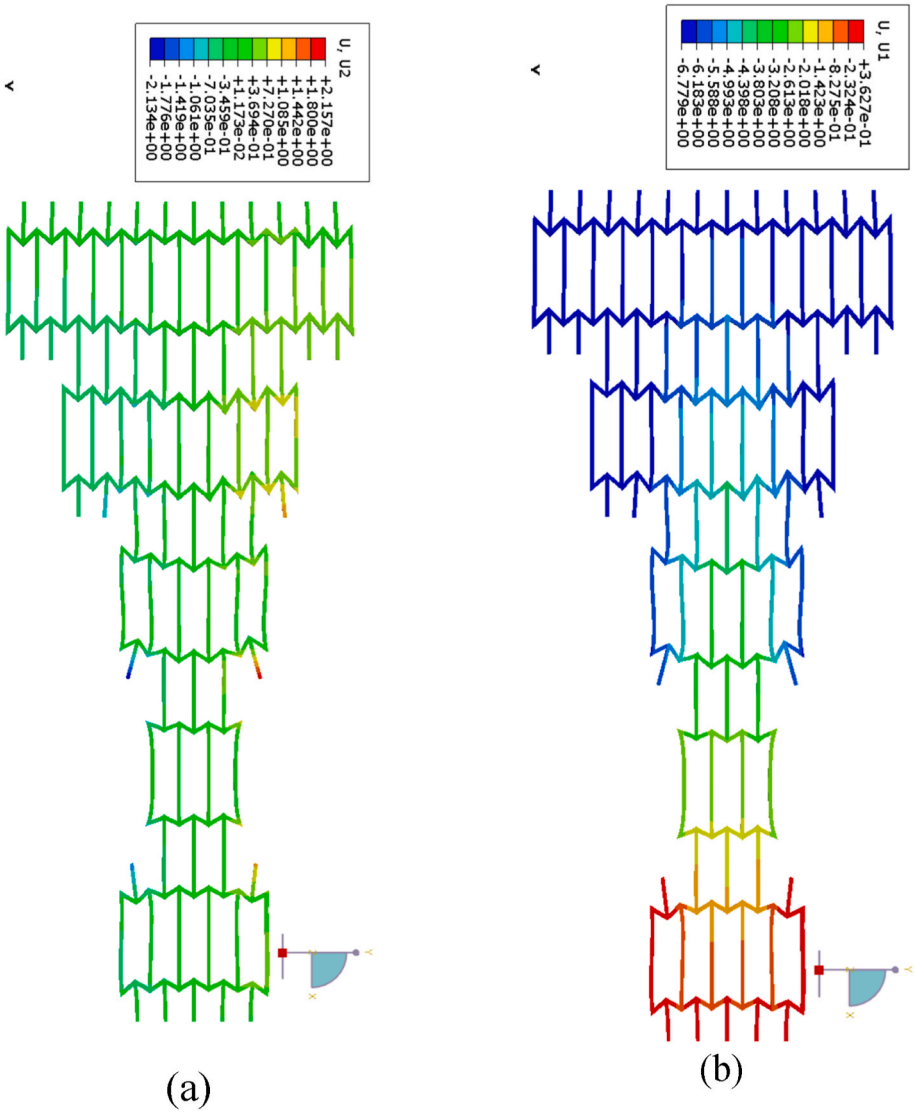

Fig. 13. (a) Transverse and (b) longitudinal displacement of the initially designed re-entrant KT.

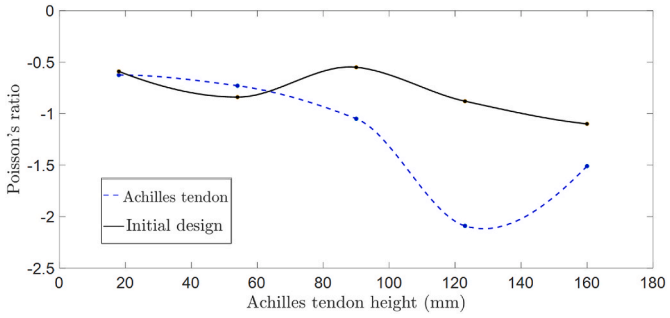

Fig. 14. Variation of Poisson's ratio of Achilles tendon and the corresponding KT model along the tendon height for a global strain of 4%.

treating Achilles tendon rupture.

Moreover, the sticky patches can be applied to the patient's skin, particularly near the parts of the body that are injured but are not necessarily open wounds, such as injured muscles or joints. The novel proposed design can facilitate the opening of microvalves due to a dynamic pressure variation due to skin density alteration (Wu et al., 2015).

Wearable devices and exo-suits clothing are promising technology as these devices help human walking by reducing the required energy consumption (Ding et al., 2018). Another potential application of the proposed design strategy is its use in developing exo-suits and wearable devices with deformations similar to the skin they are attached to. The novel re-entrant structures can help tasks such as walking, running, movement of arms, etc., and help the end-user consume less energy.

Another possible application of the presented design paradigm is auxetic on-skin sensors. The proposed design strategy in this study can be used to develop sensors for measuring the mechanical, chemical, or electrical signals or determining the pressure or strain applied to the skin or tendon (Kim et al., 2018).

4.5. Achilles tendon implant

Several researchers have examined the possibility of repairing Achilles tendons in animals (Sartori et al., 2021). For example, collagen molecules as biocompatible, biodegradable materials have been used to produce an aligned tridimensional scaffold. The tridimensional scaffold has been used as a replacement for ruptured Achilles tendons in rabbits, and the results have been desirable (Meimandi-Parizi et al., 2013). Vaughen (Vaughan, 1981) employed carbon fiber implants to repair the Achilles tendon in dogs. Despite some limitations, using carbon fiber implants was shown to be effective. In addition to animals, some

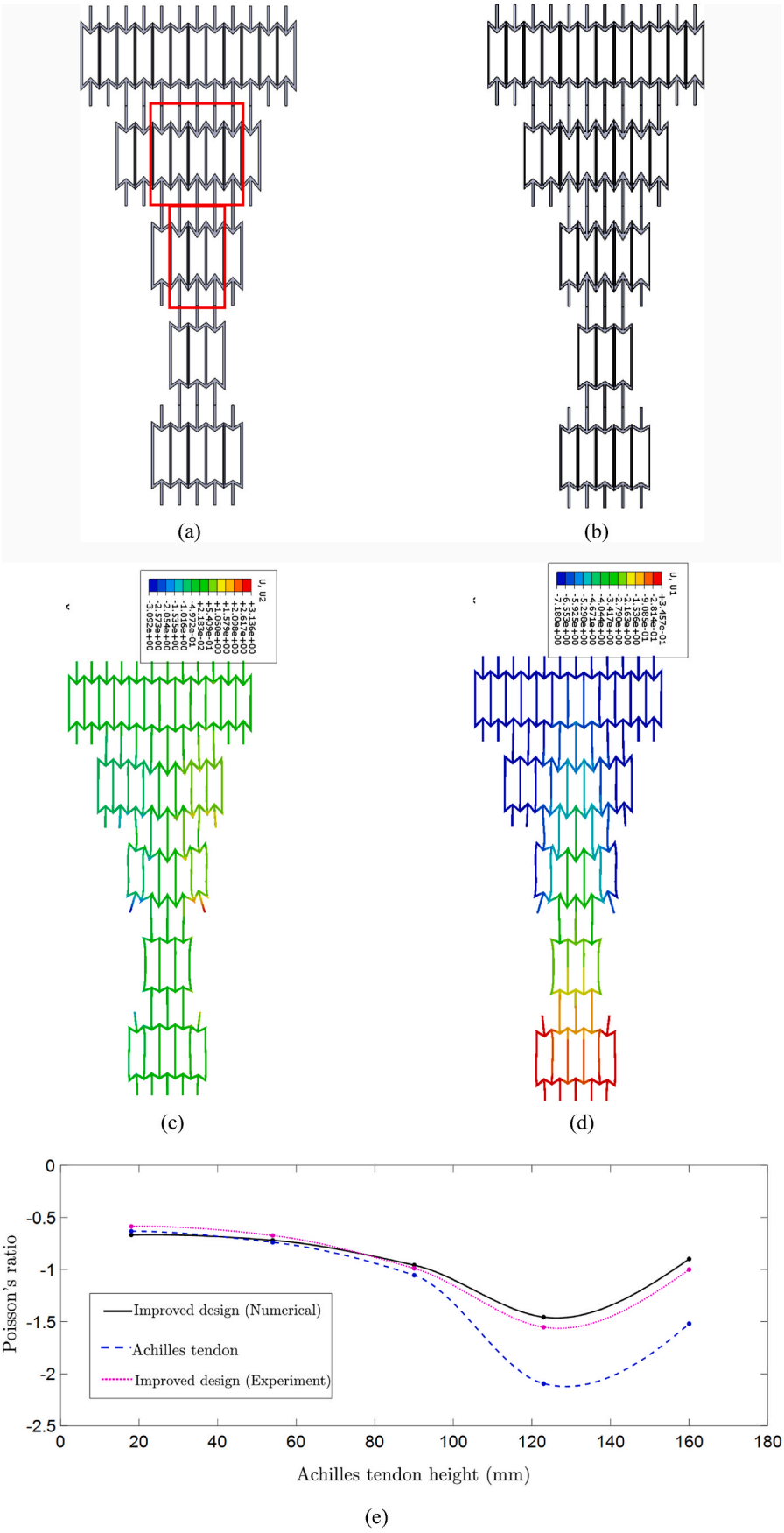

Fig. 15. (a) Cells of the initial design which were chosen to be replaced in the improved design, (b) the improved design. (c) Transverse displacement and (d) longitudinal displacement contours of the improved design. (e) Poisson's ratio vs. tendon height curves for a global strain of 4%.

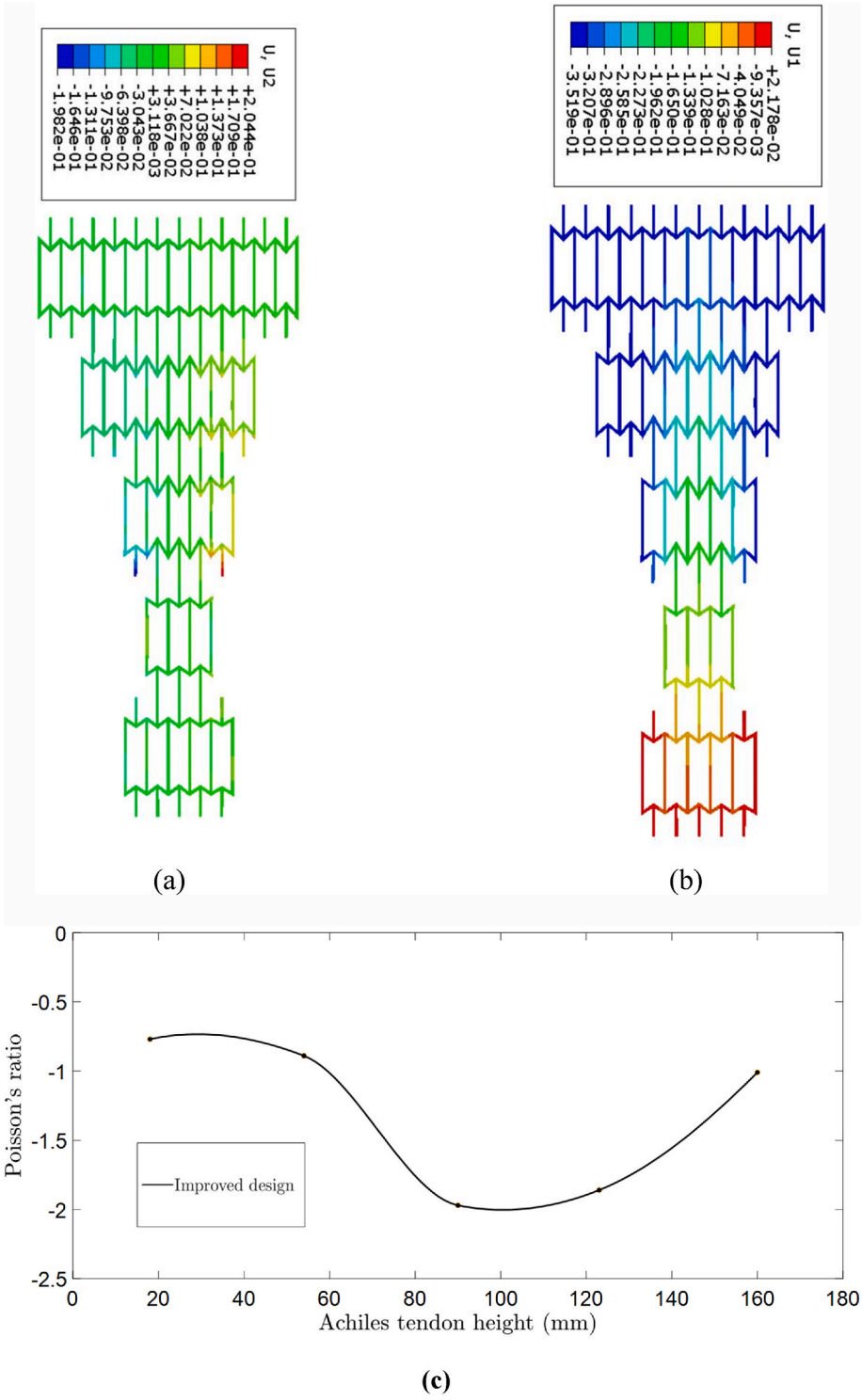

Fig. 16. (a) Transverse displacement contour, (b) longitudinal displacement contours, and (c) Poisson's ratio vs. tendon height curve for a global strain of 0.2%.

research works have been dedicated to designing and manufacturing implants to aid humans with ruptured tendons. In almost all patients, repairing flexor tendon injuries is a challenging job. In this regard, active tendon implants have been used to help patients with flexor tendon injuries. Results have shown that active tendon implants, known as Brunelli implants, are efficient, although some improvements must be made (Poggetti et al., 2018). Kempfert et al. (2022) proposed 3D-printed polycaprolactone (PCL) 2D scaffolds to be used as implants for chronic tendon ruptures as common disorders. Moreover, an attempt has been made to repair the intrasubstance Patellar tendon of humans by introducing a novel bio-inductive implant. The technique has been shown to enhance the quality of the injury repair compared to previous methods, which usually have poor quality due to the remaining tendon fibers (Bragg et al., 2022).

As discussed earlier, the re-entrant tendon design introduced in our work mimics the deformation of the Achilles tendon very well. The results of this study are expected to be instrumental in the 3D bioprinting of Achilles tendon implants. It is worth mentioning that the tensile

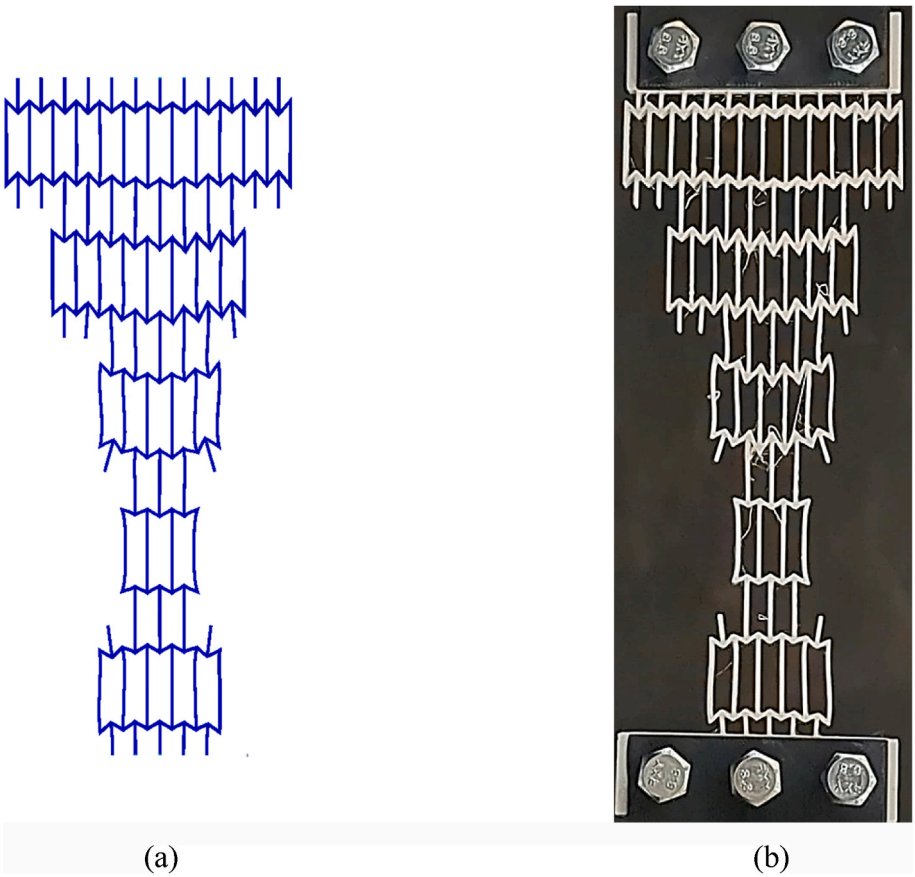

Fig. 17. Deformation of the improved re-entrant KT structure: (a) numerical model and (b) 3D printed sample.

properties of materials used for manufacturing Achilles tendon implants are crucial (Wanniarachchi et al., 2022; Erol et al., 2007), so by considering the right micro-structural dimensional parameters, the introduced design methodology can be promising for manufacturing 3D bioprinting of Achilles tendon implants.

4.6. Other materials for biomedical applications

For the present structure, TPU material was used since it has hyperelastic behavior and can recover its initial form under cyclic loading (Yousefi et al., 2023). Moreover, TPU can sustain high elongation extents before failure, which is essential for a KT application. Elastic modulus is another important mechanical property of elastomer materials for manufacturing re-entrant KT structures. Depending on the re-entrant KT structure's application, other types of elastomers can be used for manufacturing. For example, polyester urethane (PEU), polysulfide rubber, thermoplastic elastomers (TPE), Butyl rubber, and perfluoro elastomers (Visakh et al., 2013) are potential candidates in the application where the flexibility and ability to recover after large deformation are essential. Some of the noted elastomers, such as TPE, have the printability condition, while others, such as Perfluoro elastomers, do not, to the best of our knowledge. Other manufacturing technologies, such as water jetting, laser cutting, molding, etc. can be implemented in such cases. Of course, in case the implant is to be used inside the body, biocompatibility aspects must also be taken into account.

5. Conclusions

The present study is divided into two primary sections. In the first section, available analytical solutions (previous studies) for $\theta > 0$ hexagonal unit cells (honeycomb unit cells) were examined to evaluate if they are valid for $\theta < 0$ (2D re-entrant unit cells) as well. Then, new analytical relationships were proposed for hexagonal unit cells for both negative and positive ranges of θ. FEM and experimental tests were employed to evaluate and validate the proposed analytical solution. Results showed that the analytical relationships derived in this study provide the most accurate results for elastic modulus, Poisson's ratio, and yield stress compared to the previous studies. It is worth mentioning that the analytical solution proposed by some of the previous studies for yield stress is not valid for negative cell interior angle ranges (i.e., auxetics). One of the significant outcomes of the current analytical solution is good overlapping with numerical and experimental results in both the negative and positive domains of θ.

In the second section, as a practical application of the obtained results for the 2D re-entrant structure, a novel Kinesio taping (KT) with non-uniform distribution of re-entrant unit cells was designed for Achilles tendon recovery application after rupture. To this aim, the local Poisson's ratio of the tendon was determined based on the local transverse and longitudinal strains provided by DIC images of an Achilles tendon. The corresponding re-entrant angle, which gave the desired Poisson's ratio value, was determined at each position using an inverse approach. The designed novel KT was 3D printed using flexible TPU material. The numerical and experimental results demonstrated that the novel KT is capable of exhibiting a deformation similar to that of the Achilles tendon in both longitudinal and transverse directions. This feature of the re-entrant KT structure helps it attach to the skin over the Achilles tendon efficiently.

CRediT authorship contribution statement

Reza Hedayati: Validation, Methodology, Investigation, Formal

analysis, Data curation, Conceptualization, Project administration, Resources, Supervision, Visualization, Writing – original draft, Writing – review & editing. **Armin Yousefi:** Validation, Methodology, Investigation, Data curation, Conceptualization, Software, Visualization, Writing – original draft, Writing – review & editing. **Mohammadreza Lalegani Dezaki:** Methodology, Investigation, Data curation, Writing – review & editing. **Mahdi Bodaghi:** Supervision, Project administration, Methodology, Investigation, Funding acquisition, Formal analysis, Data curation, Conceptualization, Resources, Validation, Visualization, Writing – original draft, Writing – review & editing.

Declaration of competing interest

The authors declare that they have no known competing financial interests or personal relationships that could have appeared to influence the work reported in this paper.

Data availability

Data will be made available on request.

Appendix. Calculating the stiffness matrix elements

The displacements in each beam element can be decomposed into three types of deformations: (a) lateral displacement δ with no rotation, (b) rotation θ with no lateral displacement, and (c) pure axial extension. The forces and moments required to create each type of deformation are presented in Figure A18.

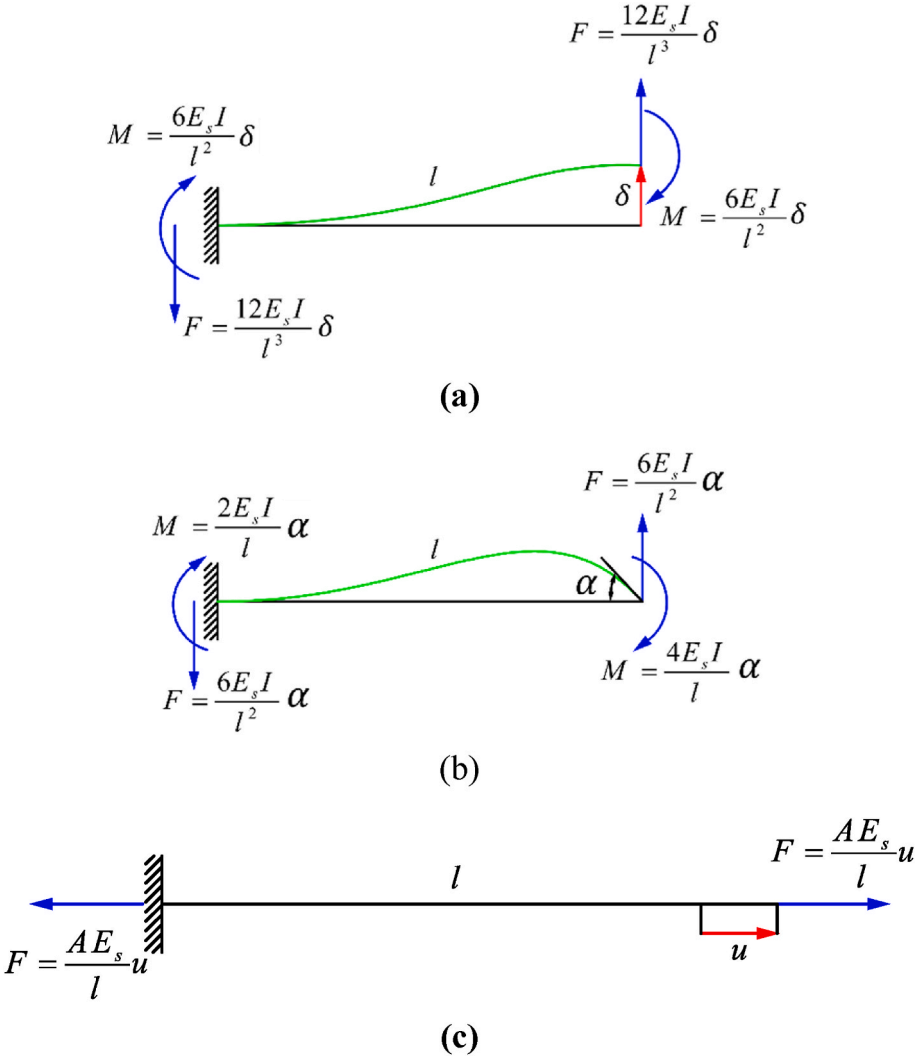

Fig. A18. Forces and moments required to create (a) lateral displacement δ with no rotation, (b) rotation θ with no lateral displacement, and (c) pure axial extension at the free end of an Euler-Bernoulli beam (Hedayati et al., 2021b),

Q_i stands for external forces applied on degree of freedom q_i. The force-displacement equation has the following form:

$$\begin{Bmatrix} Q_1 \\ Q_2 \\ Q_3 \\ Q_4 \end{Bmatrix} = \begin{bmatrix} k_{11} & k_{12} & k_{13} & k_{14} \\ k_{21} & k_{22} & k_{23} & k_{24} \\ k_{31} & k_{32} & k_{33} & k_{34} \\ k_{41} & k_{42} & k_{43} & k_{44} \end{bmatrix} \begin{Bmatrix} q_1 \\ q_2 \\ q_3 \\ q_4 \end{Bmatrix} \tag{A18}$$

In order to calculate the forces, displacement, and rotation, the stiffness matrix elements k_{ij} must be calculated. By considering the geometries in Fig. 1, it can be seen that:

$$s = \frac{1}{2}(W - H\tan\theta - h) \text{ and } l = \frac{H}{2\cos\theta}$$

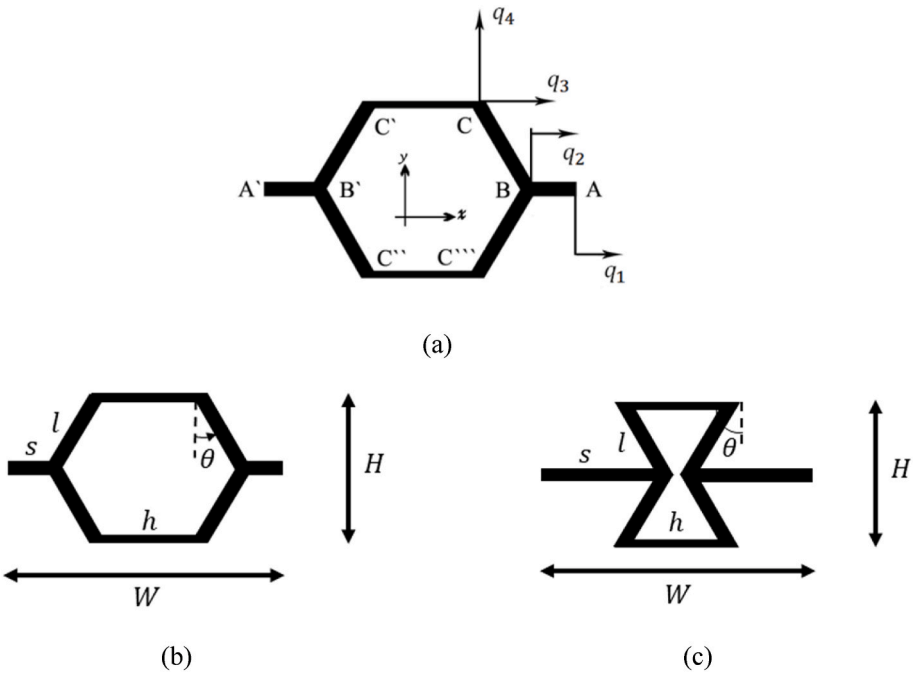

Fig. A19. (a) DOFs of a unit cell, (b) hexagonal unit cells configuration, (c) re-entrant unit cells configuration

a) $\boldsymbol{q_1 = 1}$.

In this subsection, the first column of the stiffness matrix's elements is determined by considering the displacement $q_1 = 1$ and setting $q_2 = q_3 = q_4 = 0$. This deformation displaces the right and left vertices A and A′ for unity rightwards and leftwards, respectively. Due to this deformation, strut AB is axially stretched for unity, and it applies the force $\frac{AE_s}{s}$ (see Figure A20a) on Points A and B.

To have such a deformation forces $\frac{Q_1}{2} = \frac{AE_s}{s}$ and $\frac{Q_2}{2} = -\frac{AE_s}{s}$ must be applied on vertices A and B, or in other words $Q_1 = k_{11} = \frac{2AE_s}{s}$ and $Q_2 = k_{21} = -\frac{2AE_s}{s}$. The negative value of Q_2 implies that an external load must be applied on vertex B in the opposite direction of DOF q_2 in order to keep vertex B in place. Since beams BC and CC' are not affected by this deformation mode, no external force is needed to be applied on Point C, hence $Q_3 = k_{31} = Q_4 = k_{41} = 0$.

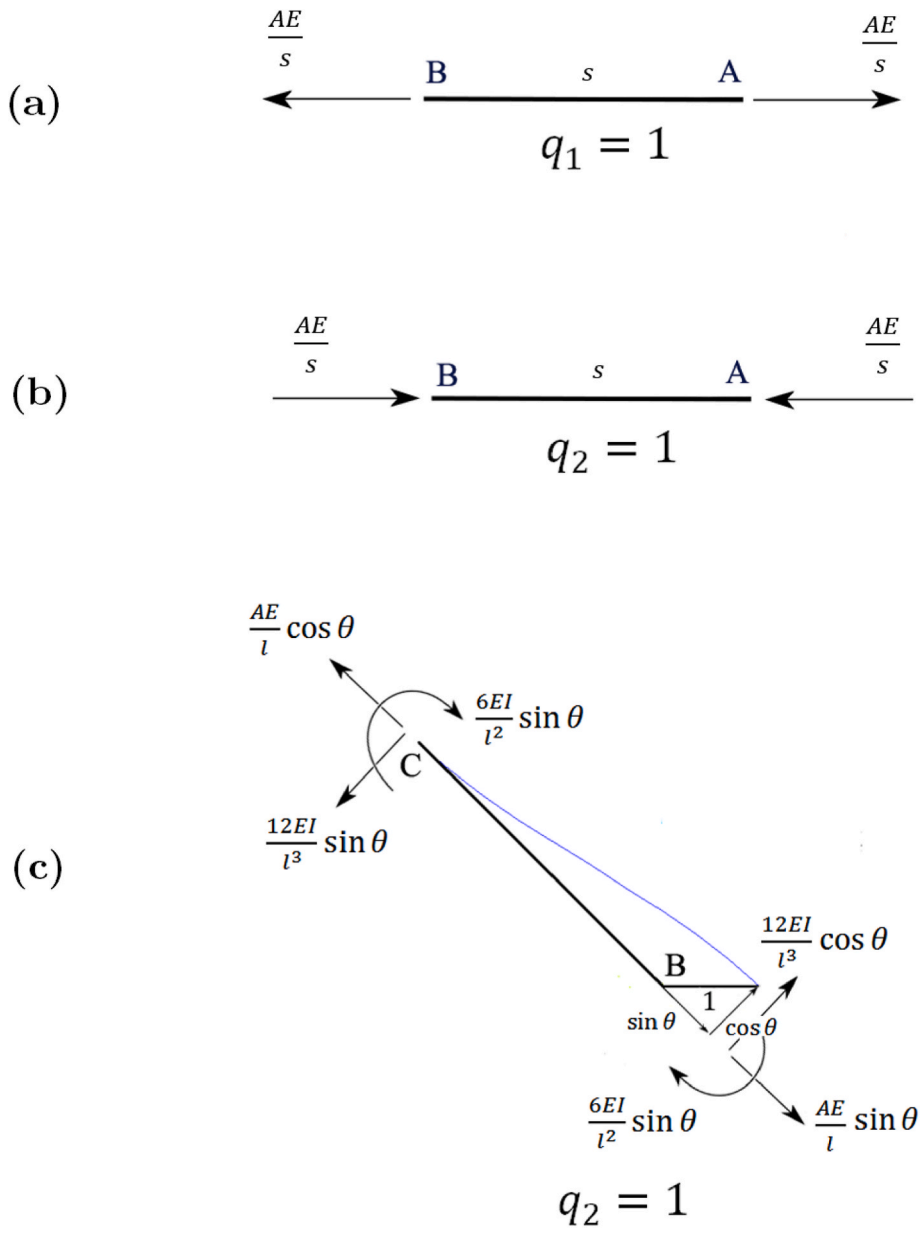

Fig. A20. Free-body diagrams of the struts (a) AB in deformation $q_1 = 1$ (b) AB in deformation $q_2 = 1$, and (c) BC in deformation $q_2 = 1$ of a hexagonal honeycomb unit cell.

b) $q_2 = 1$.

In this case, beams AB undergo pure compression, and in contrast to case $q_1 = 1$, here we have $\frac{Q_1}{2} = -\frac{AE}{s}$ (Figure A20b). Unlike the previous case, here, beam BC is deformed. Vertex A is fixed, and vertex B moves to the right side for unity. The displacement of vertex B can be decomposed into two displacements of $\cos\theta$ perpendicular to the undeformed beam BC and $\sin\theta$ along it. The axial displacements cause the force $\frac{AE}{l}\sin\theta$ and the lateral displacement impose the force $\frac{12EI}{l^3}\cos\theta$ on beam BC. Equilibrium of forces in the X direction at Point B gives (Figure A20b, c)

$$\sum f_{X,B} = 0 \quad \rightarrow -2\left(\frac{AE_s}{l}\sin^2\theta + \frac{12E_sI}{l^3}\cos^2\theta\right) - \frac{AE}{s} + \frac{Q_2}{2} = 0 \quad \rightarrow Q_3 = k_{22} = 4\left(\frac{AE_s}{l}\sin^2\theta + \frac{12E_sI}{l^3}\cos^2\theta\right) + \frac{2AE}{s} \tag{A19}$$

Beam CC' is fixed and it does not impose any force on vertex C. Similarly, the equilibrium of forces in the Y direction at Point C gives (Figure A20c)

$$\sum f_{Y,C} = 0 \quad \rightarrow -\left(\frac{AE_s}{l}\cos\theta\sin\theta - \frac{12E_sI}{l^3}\cos\theta\sin\theta\right) + \frac{Q_4}{4} = 0 \rightarrow Q_4 = k_{42} = 4\cos\theta\sin\theta\left(\frac{AE_s}{l} - \frac{12E_sI}{l^3}\right) \tag{A20}$$

and equilibrium in the X direction at vertex C gives (Figure A20)

$$\sum f_{X,C} = 0 \quad \rightarrow \frac{AE_s}{l}\cos^2\theta + \frac{12E_sI}{l^3}\sin^2\theta + \frac{Q_3}{4} = 0 \rightarrow Q_3 = k_{32} = -4\frac{AE_s}{l}\cos^2\theta - \frac{48E_sI}{l^3}\sin^2\theta \tag{A21}$$

c) $q_3 = 1$.

This deformation type displaces vertex C rightward for unity (Figure A21a). Beam AB does not deform; therefore, it does not impose any load on vertex B. Moreover, vertex A is not influenced by this deformation mode, thus $Q_1 = k_{13} = 0$. Equilibrium of forces in the X direction at Point B gives (Figure A21a)

$$\sum f_{X,B} = 0 \quad \rightarrow 2\left(\frac{AE_s}{l}\sin^2\theta + \frac{12E_sI}{l^3}\cos^2\theta\right) + \frac{Q_2}{2} = 0 \rightarrow Q_2 = k_{23} = -4\left(\frac{AE_s}{l}\sin^2\theta + \frac{12E_sI}{l^3}\cos^2\theta\right) \tag{A22}$$

Beam CC' with length h and cross-sectional area of $A/2$ is stretched for 2, and therefore it imposes the force AE_s/h on Point C. Equilibrium of forces in the X direction at Point C gives (Figure A21a)

$$\sum f_{X,C} = 0 \quad \rightarrow -\frac{AE_s}{l}\sin^2\theta - \frac{12E_sI}{l^3}\cos^2\theta - \frac{AE}{h} + \frac{Q_3}{4} = 0 \rightarrow Q_3 = k_{33} = \frac{4AE_s}{l}\sin^2\theta + \frac{48E_sI}{l^3}\cos^2\theta + \frac{4AE_s}{h} \tag{A23}$$

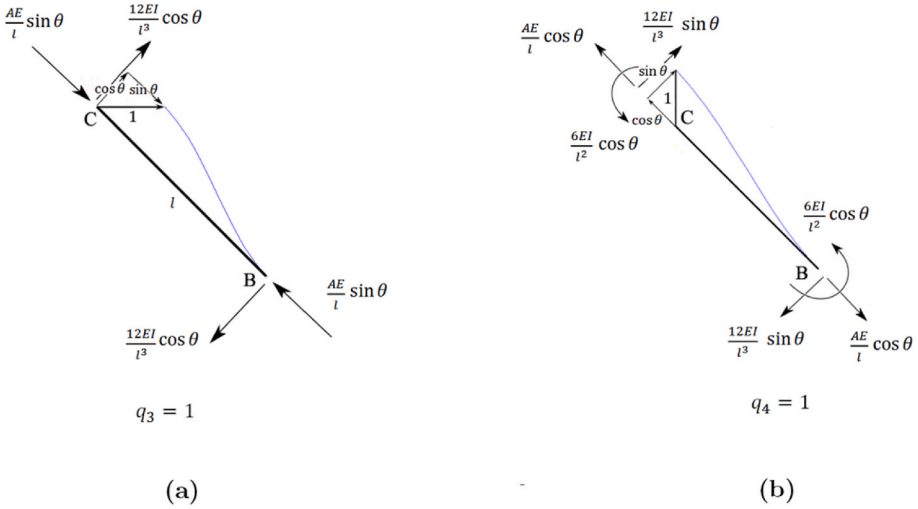

Fig. A21. Free-body diagrams of the strut BC in deformations (a $q_3 = 1$, and (b) $q_4 = 1$

Similarly, the equilibrium of forces at Point C in the Y direction gives (Figure A21a)

$$\sum f_{Y,C} = 0 \quad \rightarrow \quad \cos\theta\sin\theta\left(\frac{AE_s}{l} - \frac{12E_sI}{l^3}\right) + \frac{Q_4}{4} = 0 \rightarrow Q_4 = k_{43} = \cos\theta\sin\theta\left(\frac{48E_sI}{l^3} - \frac{4AE_s}{l}\right) \tag{A24}$$

c) $q_4 = 1$.

This deformation type displaces vertex C upwards for unity (Figure A21b). Similar to the case $q_3 = 1$, in this case we have $Q_1 = k_{14} = 0$. Equilibrium of forces at Point B in the X direction gives (Figure A21b)

$$\sum f_{X,B} = 0 \quad \rightarrow -\frac{2AE_s}{l}\cos\theta\sin\theta + \frac{24E_sI}{l^3}\cos\theta\sin\theta + \frac{Q_2}{2} = 0 \rightarrow Q_2 = k_{24} = \left(\frac{4AE_s}{l} - \frac{48E_sI}{l^3}\right)\cos\theta\sin\theta \tag{A25}$$

This time, beam CC' simply displaces without any deformation, and therefore it does not impose any load on Point C. Equilibrium of forces at Point C in the Y direction gives (Figure A21b)

$$\sum f_{Y,C} = 0 \quad \rightarrow -\frac{AE_s}{l}\cos^2\theta - \frac{12E_sI}{l^3}\sin^2\theta + \frac{Q_4}{4} = 0 \rightarrow Q_4 = k_{44} = \frac{4AE_s}{l}\cos^2\theta + \frac{48E_sI}{l^3}\sin^2\theta \tag{A26}$$

Similarly, the equilibrium of forces at Point C in the X direction gives (Figure A21b)

$$\sum f_{X,C} = 0 \quad \rightarrow \quad \cos\theta\sin\theta\left(-\frac{AE_s}{l} + \frac{12E_sI}{l^3}\right) + \frac{Q_3}{4} = 0 \rightarrow Q_3 = k_{34} = \cos\theta\sin\theta\left(\frac{48E_sI}{l^3} - \frac{4AE_s}{l}\right) \tag{A27}$$

References

Alderson, A., Alderson, K.L., Attard, D., Evans, K.E., Gatt, R., Grima, J.N., Miller, W., Ravirala, N., Smith, C., Zied, K., 2010. Elastic constants of 3-, 4-and 6-connected chiral and anti-chiral honeycombs subject to uniaxial in-plane loading. Compos. Sci. Technol. 70 (7), 1042–1048.

Bah, I., Fernandes, N.R.J., Chimenti, R.L., Ketz, J., Flemister, A.S., Buckley, M.R., 2020. Tensile mechanical changes in the Achilles tendon due to Insertional Achilles tendinopathy. J. Mech. Behav. Biomed. Mater. 112, 104031.

Baran, T., Öztürk, M., 2020. In-plane elasticity of a strengthened re-entrant honeycomb cell. Eur. J. Mech. Solid. 83, 104037.

Bragg, J.T., Shields, M.V., Salzler, M.J., 2022. Intrasubstance patellar tendon repair with the addition of a bio-inductive implant. Arthroscopy Techniques 12 (1), e11–e15.

Chansoria, P., Bonacquisti, E., Heavey, M., Le, L., Maruthamuthu, M.K., Blackwell, J., Jasiewicz, N., Sellers, R.S., Maile, R., Wallet, S., Egan, T., Nguyen, J., 2022. Instantly Adhesive and Ultra-elastic Patches for Dynamic Organ and Wound Repair. bioRxiv, p. 2022, 11.25.517820.
Chen, Z., Wu, X., Xie, Y.M., Wang, Z., Zhou, S., 2020. Re-entrant auxetic lattices with enhanced stiffness: a numerical study. Int. J. Mech. Sci. 178, 105619.
Cheng, X., Zhang, Y., Ren, X., Han, D., Jiang, W., Zhang, X.G., Luo, H.C., Xie, Y.M., 2022. Design and mechanical characteristics of auxetic metamaterial with tunable stiffness. Int. J. Mech. Sci. 223, 107286.
Craighead, D.H., Shank, S.W., Volz, K.M., Alexander, L.M., 2017. Kinesiology tape modestly increases skin blood flow regardless of tape application technique. Journal of performance health research 1.
Ding, Y., Kim, M., Kuindersma, S., Walsh, C.J., 2018. Human-in-the-loop optimization of hip assistance with a soft exosuit during walking. Science robotics 3 (15), eaar5438.
Dong, Z., Li, Y., Zhao, T., Wu, W., Xiao, D., Liang, J., 2019. Experimental and numerical studies on the compressive mechanical properties of the metallic auxetic reentrant honeycomb. Mater. Des. 182, 108036.
Erol, B., Kocaoğlu, B., Esemenli, T., 2007. Spiral-shaped metallic implant in the treatment of Achilles tendon ruptures: an experimental study on the Achilles tendon of sheep. J. Foot Ankle Surg. 46 (3), 155–161.
Evans, K.E., Alderson, A., 2000. Auxetic materials: functional materials and structures from lateral thinking! Adv. Mater. 12 (9), 617–628.
Fozdar, D.Y., Soman, P., Lee, J.W., Han, L.H., Chen, S., 2011. Three-dimensional polymer constructs exhibiting a tunable negative Poisson's ratio. Adv. Funct. Mater. 21 (14), 2712–2720.
Fu, M., Xu, O., Hu, L., Yu, T., 2016. Nonlinear shear modulus of re-entrant hexagonal honeycombs under large deformation. Int. J. Solid Struct. 80, 284–296.
Gatt, R., Wood, M.V., Gatt, A., Zarb, F., Formosa, C., Azzopardi, K.M., Casha, A., Agius, T. P., Schembri-Wismayer, P., Attard, L., 2015. Negative Poisson's ratios in tendons: an unexpected mechanical response. Acta Biomater. 24, 201–208.
Ghavidelnia, N., Hedayati, R., Sadighi, M., Mohammadi-Aghdam, M., 2020a. Development of porous implants with non-uniform mechanical properties distribution based on CT images. Appl. Math. Model. 83, 801–823.
Ghavidelnia, N., Jedari Salami, S., Hedayati, R., 2020b. Analytical Relationships for Yield Stress of Five Mechanical Meta-Biomaterials. Mechanics Based Design of Structures and Machines, pp. 1–23.
Ghavidelnia, N., Bodaghi, M., Hedayati, R., 2021. Idealized 3D auxetic mechanical metamaterial: an analytical, numerical, and experimental study. Materials 14 (4), 993.
Gibson, L.J., Ashby, M.F., 1999. Cellular Solids: Structure and Properties. Cambridge university press.
Gupta, S., Gupta, V., Chanda, A., 2022. Biomechanical modeling of novel high expansion auxetic skin grafts. International Journal for Numerical Methods in Biomedical Engineering e3586.
Haen, T.X., Roux, A., Soubeyrand, M., Laporte, S., 2017. Shear waves elastography for assessment of human Achilles tendon's biomechanical properties: an experimental study. J. Mech. Behav. Biomed. Mater. 69, 178–184.
Hedayati, R., Lakshmanan, S., 2020. Pneumatically-actuated acoustic metamaterials based on helmholtz resonators. Materials 13 (6), 1456.
Hedayati, R., Sadighi, M., Mohammadi Aghdam, M., Zadpoor, A.A., 2016. Mechanical properties of additively manufactured thick honeycombs. Materials 9 (8), 613.
Hedayati, R., Mirzaali, M., Vergani, L., Zadpoor, A., 2018. Action-at-a-distance metamaterials: distributed local actuation through far-field global forces. Apl. Mater. 6 (3), 036101.
Hedayati, R., Güven, A., Van Der Zwaag, S., 2021a. 3D gradient auxetic soft mechanical metamaterials fabricated by additive manufacturing. Appl. Phys. Lett. 118 (14), 141904.
Hedayati, R., Ghavidelnia, N., Sadighi, M., Bodaghi, M., 2021b. Improving the accuracy of analytical relationships for mechanical properties of permeable metamaterials. Appl. Sci. 11 (3), 1332.
Hedayati, R., Roudbarian, N., Tahmasiyan, S., Bodaghi, M., 2023. Gradient origami metamaterials for programming out-of-plane curvatures. Adv. Eng. Mater,, 2201838.
Hu, L., Zhou, M.Z., Deng, H., 2018. Dynamic crushing response of auxetic honeycombs under large deformation: theoretical analysis and numerical simulation. Thin-Walled Struct. 131, 373–384.
Huang, C.-Y., Hsieh, T.-H., Lu, S.-C., Su, F.-C., 2011. Effect of the Kinesio tape to muscle activity and vertical jump performance in healthy inactive people. Biomed. Eng. Online 10 (1), 1–11.
Huang, H.H., Wong, B.L., Chou, Y.C., 2016. Design and properties of 3D-printed chiral auxetic metamaterials by reconfigurable connections. Phys. Status Solidi 253 (8), 1557–1564.
Kamrava, S., Mousanezhad, D., Ebrahimi, H., Ghosh, R., Vaziri, A., 2017. Origami-based cellular metamaterial with auxetic, bistable, and self-locking properties. Sci. Rep. 7 (1), 1–9.
Kempfert, M., Willbold, E., Loewner, S., Blume, C., Pitts, J., Menzel, H., Roger, Y., Hoffmann, A., Angrisani, N., Reifenrath, J., 2022. Polycaprolactone-based 3D-printed scaffolds as potential implant materials for tendon-defect repair. J. Funct. Biomater. 13 (4), 160.
Kharazi, M., Bohm, S., Theodorakis, C., Mersmann, F., Arampatzis, A., 2021. Quantifying mechanical loading and elastic strain energy of the human Achilles tendon during walking and running. Sci. Rep. 11 (1), 1–13.
Kim, H.W., Kim, T.Y., Park, H.K., You, I., Kwak, J., Kim, J.C., Hwang, H., Kim, H.S., Jeong, U., 2018. Hygroscopic auxetic on-skin sensors for easy-to-handle repeated daily use. ACS Appl. Mater. Interfaces 10 (46), 40141–40148.
Kolken, H.M., Zadpoor, A., 2017. Auxetic mechanical metamaterials. RSC Adv. 7 (9), 5111–5129.
Kolken, H.M., Janbaz, S., Leeflang, S.M., Lietaert, K., Weinans, H.H., Zadpoor, A.A., 2018. Rationally designed meta-implants: a combination of auxetic and conventional meta-biomaterials. Mater. Horiz. 5 (1), 28–35.
Kolken, H.M.A., Lietaert, K., van der Sloten, T., Pouran, B., Meynen, A., Van Loock, G., Weinans, H., Scheys, L., Zadpoor, A.A., 2020. Mechanical performance of auxetic meta-biomaterials. J. Mech. Behav. Biomed. Mater. 104, 103658.
Kolken, H.M.A., Garcia, A.F., Du Plessis, A., Rans, C., Mirzaali, M.J., Zadpoor, A.A., 2021. Fatigue performance of auxetic meta-biomaterials. Acta Biomater. 126, 511–523.
Lee, J.-h., Yoo, W.-g., 2012. Treatment of chronic Achilles tendon pain by Kinesio taping in an amateur badminton player. Phys. Ther. Sport 13 (2), 115–119.
Ling, B., Wei, K., Wang, Z., Yang, X., Qu, Z., Fang, D., 2020. Experimentally program large magnitude of Poisson's ratio in additively manufactured mechanical metamaterials. Int. J. Mech. Sci. 173, 105466.
Lorato, A., Innocenti, P., Scarpa, F., Alderson, A., Alderson, K., Zied, K., Ravirala, N., Miller, W., Smith, C., Evans, K., 2010. The transverse elastic properties of chiral honeycombs. Compos. Sci. Technol. 70 (7), 1057–1063.
Lu, Z.-X., Li, X., Yang, Z.-Y., Xie, F., 2016. Novel structure with negative Poisson's ratio and enhanced Young's modulus. Compos. Struct. 138, 243–252.
Lv, C., Krishnaraju, D., Konjevod, G., Yu, H., Jiang, H., 2014. Origami based mechanical metamaterials. Sci. Rep. 4, 5979.
Lyman, K.J., Keister, K., Gange, K., Mellinger, C.D., Hanson, T.A., 2017. Investigating the effectiveness of KINESIO® taping space correction method in healthy adults on patellofemoral joint and subcutaneous space. Int J Sports Phys Ther 12 (2), 250–257.
Masters, I., Evans, K., 1996. Models for the elastic deformation of honeycombs. Compos. Struct. 35 (4), 403–422.
Meeusen, L., Candidori, S., Micoli, L.L., Guidi, G., Stanković, T., Graziosi, S., 2022a. Auxetic structures used in kinesiology tapes can improve form-fitting and personalization. Sci. Rep. 12 (1), 13509.
Meeusen, L., Candidori, S., Micoli, L.L., Guidi, G., Stanković, T., Graziosi, S., 2022b. Auxetic structures used in kinesiology tapes can improve form-fitting and personalization. Sci. Rep. 12 (1), 1–13.
Meimandi-Parizi, A., Oryan, A., Moshiri, A., 2013. Tendon tissue engineering and its role on healing of the experimentally induced large tendon defect model in rabbits: a comprehensive in vivo study. PLoS One 8 (9), e73016.
Mirzaali, M., Hedayati, R., Vena, P., Vergani, L., Strano, M., Zadpoor, A., 2017. Rational design of soft mechanical metamaterials: independent tailoring of elastic properties with randomness. Appl. Phys. Lett. 111 (5), 051903.
Morais, D.S., Cruz, J., Fangueiro, R., Lopes, H., Guedes, R.M., Lopes, M.A., 2020. Mechanical behavior of ropes based on polypropylene (PP) and poly(ethylene terephthalate) (PET) multifilament yarns for Achilles tendon partial substitution. J. Mech. Behav. Biomed. Mater. 106, 103734.
Nagelli, C.V., Hooke, A., Quirk, N., De Padilla, C.L., Hewett, T.E., van Griensven, M., Coenen, M., Berglund, L., Evans, C.H., Mueller, S., 2021. Mechanical and Possible Auxetic Properties of Human Achilles Tendon during in Vitro Testing to Failure bioRxiv.
Nagelli, C., Hooke, A., Quirk, N., De Padilla, C., Hewett, T., van Griensven, M., Coenen, M., Berglund, L., Evans, C., Müller, S., 2022. Mechanical and strain behaviour of human Achilles tendon during in vitro testing to failure. Eur. Cell. Mater. 43, 153–161.
Nicolaou, Z.G., Motter, A.E., 2012. Mechanical metamaterials with negative compressibility transitions. Nat. Mater. 11 (7), 608–613.
Notermans, T., Khayyeri, H., Isaksson, H., 2019. Understanding how reduced loading affects Achilles tendon mechanical properties using a fibre-reinforced poro-visco-hyper-elastic model. J. Mech. Behav. Biomed. Mater. 96, 301–309.
Ohtaki, H., Hu, G., Nagasaka, Y., Kotosaka, S., 2004. Analysis of negative Poisson's ratios of Re-entrant honeycombs. JSME International Journal Series A Solid Mechanics and Material Engineering 47 (2), 113–121.
Pan, Q., Chen, S., Chen, F., Zhu, X., 2020. Programmable Soft Bending Actuators with Auxetic Metamaterials. Science China Technological Sciences, pp. 1–9.
Poggetti, A., Novi, M., Rosati, M., Ciclamini, D., Scaglione, M., Battiston, B., 2018. Treatment of flexor tendon reconstruction failures: multicentric experience with Brunelli active tendon implant. Eur. J. Orthop. Surg. Traumatol. 28 (5), 877–883.
Rafsanjani, A., Pasini, D., 2016. Bistable auxetic mechanical metamaterials inspired by ancient geometric motifs. Extreme Mechanics Letters 9, 291–296.
Roudbarian, N., Jebellat, E., Famouri, S., Baniasadi, M., Hedayati, R., Baghani, M., 2022. Shape-memory polymer metamaterials based on triply periodic minimal surfaces. Eur. J. Mech. Solid. 96, 104676.
Sartori, J., Köhring, S., Bruns, S., Moosmann, J., Hammel, J.U., 2021. Gaining insight into the deformation of achilles tendon entheses in mice. Adv. Eng. Mater. 23 (11), 2100085.
Schneebeli, A., Falla, D., Clijsen, R., Barbero, M., 2020. Myotonometry for the evaluation of Achilles tendon mechanical properties: a reliability and construct validity study. BMJ Open Sport & Exercise Medicine 6 (1), e000726.
Sedal, A., Fisher, M., Bishop-Moser, J., Wineman, A., Kota, S., 2018. Auxetic sleeves for soft actuators with kinematically varied surfaces. In: 2018 IEEE/RSJ International Conference on Intelligent Robots and Systems (IROS). IEEE.
Serjouei, A., Yousefi, A., Jenaki, A., Bodaghi, M., Mehrpouya, M., 2022. 4D printed shape memory sandwich structures: experimental analysis and numerical modeling. Smart Mater. Struct. 31 (5), 055014.
Shirzad, M., Zolfagharian, A., Matbouei, A., Bodaghi, M., 2021. Design, evaluation, and optimization of 3D printed truss scaffolds for bone tissue engineering. J. Mech. Behav. Biomed. Mater. 120, 104594.
Skirven, T.M., Osterman, A.L., Fedorczyk, J., Amadio, P.C., 2011. Rehabilitation of the Hand and Upper Extremity, 2-volume Set E-Book: Expert Consult. Elsevier Health Sciences.

Slann, A., White, W., Scarpa, F., Boba, K., Farrow, I., 2015. Cellular plates with auxetic rectangular perforations. Phys. Status Solidi 252 (7), 1533–1539.
Sprague, A.L., Awokuse, D., Pohlig, R.T., Cortes, D.H., Grävare Silbernagel, K., 2020. Relationship between mechanical properties (shear modulus and viscosity), age, and sex in uninjured Achilles tendons. Translational sports medicine 3 (4), 321–327.
Standard, A., 2010. D638-10. Standard Test Methods for Tensile Properties of Plastics. ASTM International, West Conshohocken, PA.
Tarantino, D., Palermi, S., Sirico, F., Corrado, B., 2020. Achilles tendon rupture: mechanisms of injury, principles of rehabilitation and return to play. Journal of functional morphology and kinesiology 5 (4), 95.
Vaughan, L., 1981. The use of carbon fibre implants for the repair of Achilles tendon rupture in dogs. J. Small Anim. Pract. 22 (10), 629–634.
Veisi, H., Farrokhabadi, A., 2021. Investigation of the equivalent material properties and failure stress of the re-entrant composite lattice structures using an analytical model. Compos. Struct. 257, 113161.
Vellaparambil, R., Han, W.-S., Di Giovanni, P., Avril, S., 2023. Potential of auxetic designs in endovascular aortic repair: a computational study of their mechanical performance. J. Mech. Behav. Biomed. Mater. 138, 105644.
Visakh, P., Thomas, S., Chandra, A.K., Mathew, A.P., 2013. Advances in Elastomers. Springer2013.
Wan, H., Ohtaki, H., Kotosaka, S., Hu, G., 2004. A study of negative Poisson's ratios in auxetic honeycombs based on a large deflection model. Eur. J. Mech. Solid. 23 (1), 95–106.
Wang, Z., Hu, H., 2014. Auxetic materials and their potential applications in textiles. Textil. Res. J. 84 (15), 1600–1611.
Wang, H., Lu, Z., Yang, Z., Li, X., 2019. A novel re-entrant auxetic honeycomb with enhanced in-plane impact resistance. Compos. Struct. 208, 758–770.
Wanniarachchi, C.T., Arjunan, A., Baroutaji, A., Singh, M., 2022. Mechanical performance of additively manufactured cobalt-chromium-molybdenum auxetic meta-biomaterial bone scaffolds. J. Mech. Behav. Biomed. Mater. 134, 105409.
Warner, J.J., Gillies, A.R., Hwang, H.H., Zhang, H., Lieber, R.L., Chen, S., 2017. 3D-printed biomaterials with regional auxetic properties. J. Mech. Behav. Biomed. Mater. 76, 145–152.
Whitty, J., Nazare, F., Alderson, A., 2002. Modelling the effects of density variations on the in-plane Poisson's ratios and Young's moduli of periodic conventional and re-entrant honeycombs-Part 1: rib thickness variations. Cell. Polym. 21 (2), 69–98.
Wu, W.-T., Hong, C.-Z., Chou, L.-W., 2015. The kinesio taping method for myofascial pain control. Evid. base Compl. Alternative Med. 2015.
Xu, H.H., Luo, H.C., Zhang, X.G., Jiang, W., Teng, X.C., Chen, W.Q., Yang, J., Xie, Y.M., Ren, X., 2023. Mechanical properties of aluminum foam filled re-entrant honeycomb with uniform and gradient designs. Int. J. Mech. Sci. 244, 108075.
Yin, N.-H., Fromme, P., McCarthy, I., Birch, H.L., 2021. Individual variation in Achilles tendon morphology and geometry changes susceptibility to injury. Elife 10, e63204.
Yousefi, A., Jolaiy, S., Dezaki, M.L., Zolfagharian, A., Serjouei, A., Bodaghi, M., 2023. 3D printed soft and hard meta-structures with supreme energy absorption and dissipation capacities in cyclic loading conditions. Adv. Eng. Mater. 25 (4), 2201189.
Zeng, Q., Zhao, Z., Lei, H., Wang, P., 2023. A deep learning approach for inverse design of gradient mechanical metamaterials. Int. J. Mech. Sci. 240, 107920.